Journal Pre-proofs

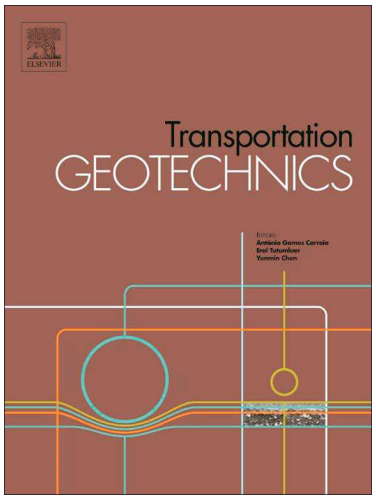

Emulating long-term weather-driven transportation earthworks deterioration models to support asset management

P.R. Helm, A. Svalova, A.M. Morsy, M. Rouainia, A. Smith, A. El-Hamalawi, D.J. Wilkinson, H. Postill, S. Glendinning

PII: S2214-3912(23)00228-3
DOI: https://doi.org/10.1016/j.trgeo.2023.101155
Reference: TRGEO 101155

To appear in: *Transportation Geotechnics*

Received Date: 29 April 2023
Revised Date: 4 November 2023
Accepted Date: 18 November 2023

Please cite this article as: P.R. Helm, A. Svalova, A.M. Morsy, M. Rouainia, A. Smith, A. El-Hamalawi, D.J. Wilkinson, H. Postill, S. Glendinning, Emulating long-term weather-driven transportation earthworks deterioration models to support asset management, *Transportation Geotechnics* (2023), doi: https://doi.org/10.1016/j.trgeo.2023.101155

Emulating long-term weather-driven transportation earthworks deterioration models to support asset management.

Helm, P.R.[a]; Svalova, A.[b]; Morsy, A.M.[c,1,2]; Rouainia, M.[a]; Smith, A.[c]; El-Hamalawi, A.[c]; Wilkinson, D.J.[d]; Postill, H.[c,2]; Glendinning, S.[a]

Author Affiliations:

[a] Newcastle University, School of Engineering, Newcastle upon Tyne, NE1 7RU, UK.

[b] Newcastle University, School of Mathematics, Statistics and Physics, Newcastle upon Tyne, NE1 7RU, UK.

[c] Loughborough University, School of Architecture, Building and Civil Engineering, Loughborough, LE11 3TU, UK.

[d] Durham University, Department of Mathematical Sciences, Durham, DH1 3LE, UK.

[1] California State University Long Beach, Department of Civil Engineering and Construction Engineering Management, Long Beach, CA 90840, USA.

[2] Formerly of Loughborough University.

Corresponding author: peter.helm@ncl.ac.uk

Address: Civil and Geospatial Engineering, School of Engineering, Second Floor, Cassie Building, Newcastle University, Newcastle upon Tyne, NE1 7RU, United Kingdom.

Keywords: Slope stability; Numerical modeling; Statistical emulation; Deterioration; Earthworks

Abstract:

The deterioration of transport infrastructure earthworks is a global problem, with negative impacts for infrastructure resilience, becoming of increasing significance as existing infrastructure ages. Key mechanisms which affect this deterioration include seasonal pore pressure cycling driven by changing weather and climate, and the long-term dissipation of construction induced excess pore pressures. These complex processes lead to significant uncertainty in rates of deterioration and the current state of existing earthworks assets. The objective in this work was to establish a framework to emulate deterministic numerical models of slope deterioration over time using statistical (Gaussian process) emulation. A validated, physically based, deterministic modeling capability has been developed that can replicate the hydro-mechanically coupled

behavior of cut and embankment slopes and their deterioration as driven by weather and climate. In parallel, a statistical (Gaussian process) emulator model was developed, and then trained with data from a deterministic modeling parametric study, using a formal experimental design approach, making use of Latin hypercube sampling. Exemplar forecasting outputs are presented to demonstrate application of the approach for use in decision-making. This information can be used in the design of new earthworks and the management of existing earthwork portfolios.

1 Introduction

Weather-driven cycles of pore pressure can cause deterioration of soils and earthworks [1], and these cycles are thought to cause an increase in the void ratio of compacted fills [2]. Slope vegetation also plays a key role in slope surface-atmosphere interaction [3], having significant impacts on the magnitude of seasonal pore pressure cycles. Climate change in the UK is likely to exacerbate these issues due to the change in the seasonal distribution of wetting and drying and the increased magnitude of seasonal cycle size [4], along with the additional uncertainty posed by both the variability of future climate projections [5] and the potential effect any future change may have on infrastructure. Climate change, and the resultant effects on weather are also projected to occur both in Europe [6], and globally [7]. These changes are likely to have negative effects on geotechnical infrastructure [8] with rail transport infrastructure in Europe thought to be at particularly high risk from extreme weather events [6]. Climate change and extreme weather events have also been recognized as a significant potential risk to transport infrastructure in the US [9,10].

Earthworks form a key part of transport infrastructure worldwide [8] and their stability, or lack thereof, can cause significant safety and serviceability issues. In the UK, Network Rail manages over 19,000 km of earthwork slopes [11] and National Highways manage 46,900 individual earthworks [12]. Significant railway construction in the UK began in the 1830s [13], and Network Rail estimate that the majority of their earthworks are over 150 years old with the age of earthworks in some parts of the network exceeding 170 years [11]. These slopes have therefore undergone large numbers of wet-dry cycles, deteriorating to an unknown magnitude. Further uncertainty is added by construction being undertaken before a modern understanding of soil mechanics, leading to a number of issues, including; lack of compaction in embankments (along with the use of end tipping to place fill and/or compaction by horse runs); a lack of foundation preparation [14–16] and; the over steepening of both embankment and cutting slopes compared to those engineered more recently. This poses a problem for asset owners who are dealing with spatially and temporally diverse assets.

The UK trunk road and highways network is significantly younger than the railway network with initial motorway construction commencing in 1956 and the first major phase of motorway construction starting in the 1960s [17]. As such UK highways geotechnical infrastructure tends to be no more than 65 years old and has the benefit of being designed and constructed with a modern understanding of soil mechanics, making use of modern excavation and compaction equipment allowing the removal of greater volumes of material and achieving better and more consistent compaction of fill. As such, UK highways slopes tend to be less steep, and more homogeneous (in the case of embankments) than the 19th century rail slopes [16,18].

At present Network Rail and UK National Highways do not specify a design life for geotechnical infrastructure, instead stating that earthworks are a "*long life asset*" [11] or that geotechnical assets are typically expected to have a "*long service life*" [19]. However Network Rail specify a 20 year and 120 year serviceable life for "refurbished" and "renewed" earthworks assets [20], and guidance in publications relating to UK highways quotes values of 60+ years for design life and 120+ years for effective service life [12].

A key aim of the UK government is to improve resilience of infrastructure, and it has been identified by the UK National Infrastructure Commission [NIC, 21] that "*…predictive asset management models, could provide more detailed information on asset condition and performance, helping to prevent failures and better target maintenance interventions or renewals*". As such an understanding of the current state of deterioration and how that might change over time is needed for improved asset management both now and in the future.

Addressing the need for models to predict changing asset condition was the focus of this study, with application to transport infrastructure earthworks.

The objective was to establish a framework to emulate deterministic numerical models of slope deterioration over time using Gaussian processes (GPs). The GPs provide not only a fast surrogate for the computationally expensive deterministic numerical models, but also properly quantify and propagate uncertainty associated with the statistical approximation. Development and validation of the deterministic numerical models, and development of the statistical emulator, are described. Exemplar forecasting outputs are presented to demonstrate application of the approach for use in decision-making.

2 Modeling framework and experimental design

This paper draws together an existing body of work that has been used to produce data that allows the characterization of the changing state of an earthworks asset or group of assets due to deterioration, in line with the requirements outlined by the UK NIC. The workflow required to derive the deterioration data is summarized in Figure 1 and the steps to produce the asset and network scale deterioration data are described in more detail in this publication.

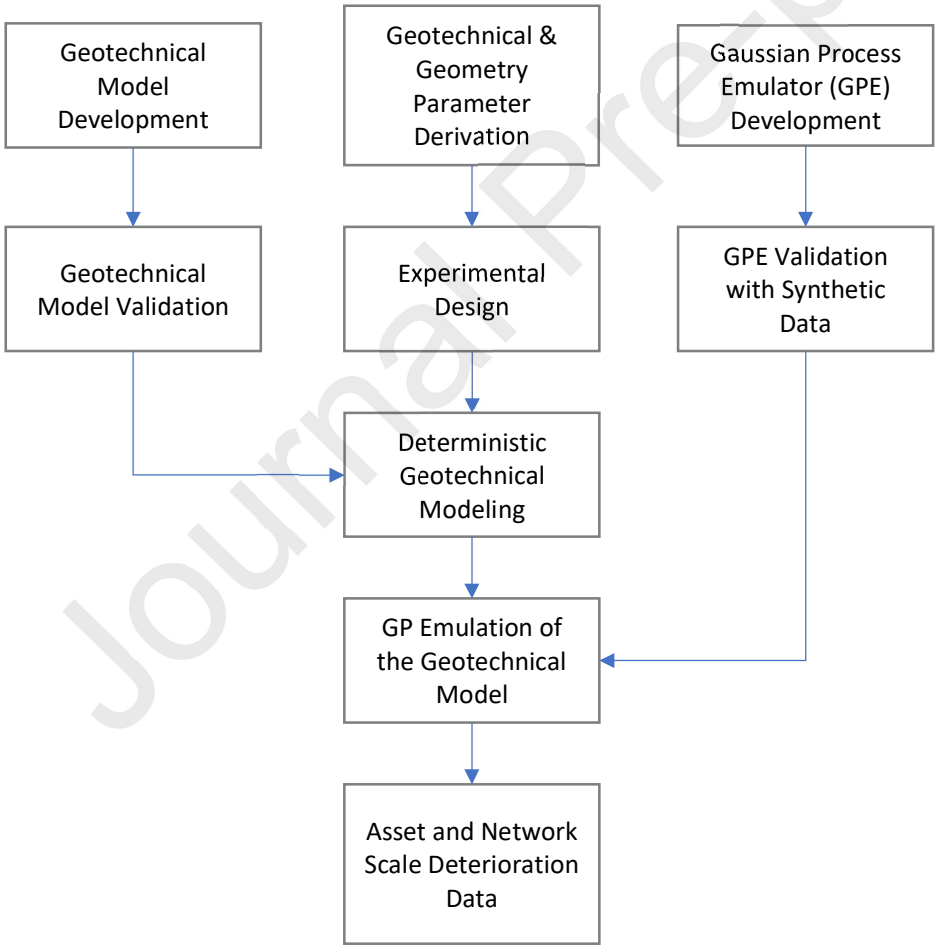

Figure 1: Diagram showing the workflow required to produce asset and network scale deterioration data by the emulator.

2.1 Experimental design

In order to undertake GP emulation [22,23], a Latin hypercube sampling (LHS) approach has been adopted for the experimental design. This is widely used in the statistical design of experiments [24] but is not commonly used in geotechnical engineering, although examples of the approach being adopted are beginning to be appear, see for example Xu and Wang [25].

An LHS design approach optimizes coverage of a parameter space (i.e., range of parameters) with the minimum number of experiments. Each parameter to be varied (e.g., apparent cohesion, friction angle etc.), corresponds to a dimension of the hypercube, and said dimension is discretized into a number of equal sized bins set equal to the total number of experiments to be undertaken. For each bin and dimension, parameter values are randomly sampled from a uniform distribution with the condition that each bin can only be selected once. Therefore, each experiment (or model) run corresponds to a unique parameter ensemble, and across the full set of experiment runs, no parameter values are repeated, leading to an efficient sampling of the parameter space. These designs "fill space" much more efficiently than more naïve parameter scans and factorial designs. For a more thorough treatment of formal experimental design approaches and LHS see Santner et al. [24].

The LHS adopts a maximin sampling criterion which maximizes the minimum distance between sample points, while placing the sampled point in a randomized location within a sample interval [26]. Once the samples have been drawn for each dimension, they must be transformed to derive the deterministic model input parameters. The adopted LHS output vectors are summarized in Figure 2 where it can be seen that for a given model there is a single value for each of the adopted parameters and that those values are never repeated in any of the other models. The LHS design array is then used to allocate the appropriate parameters to each of the models.

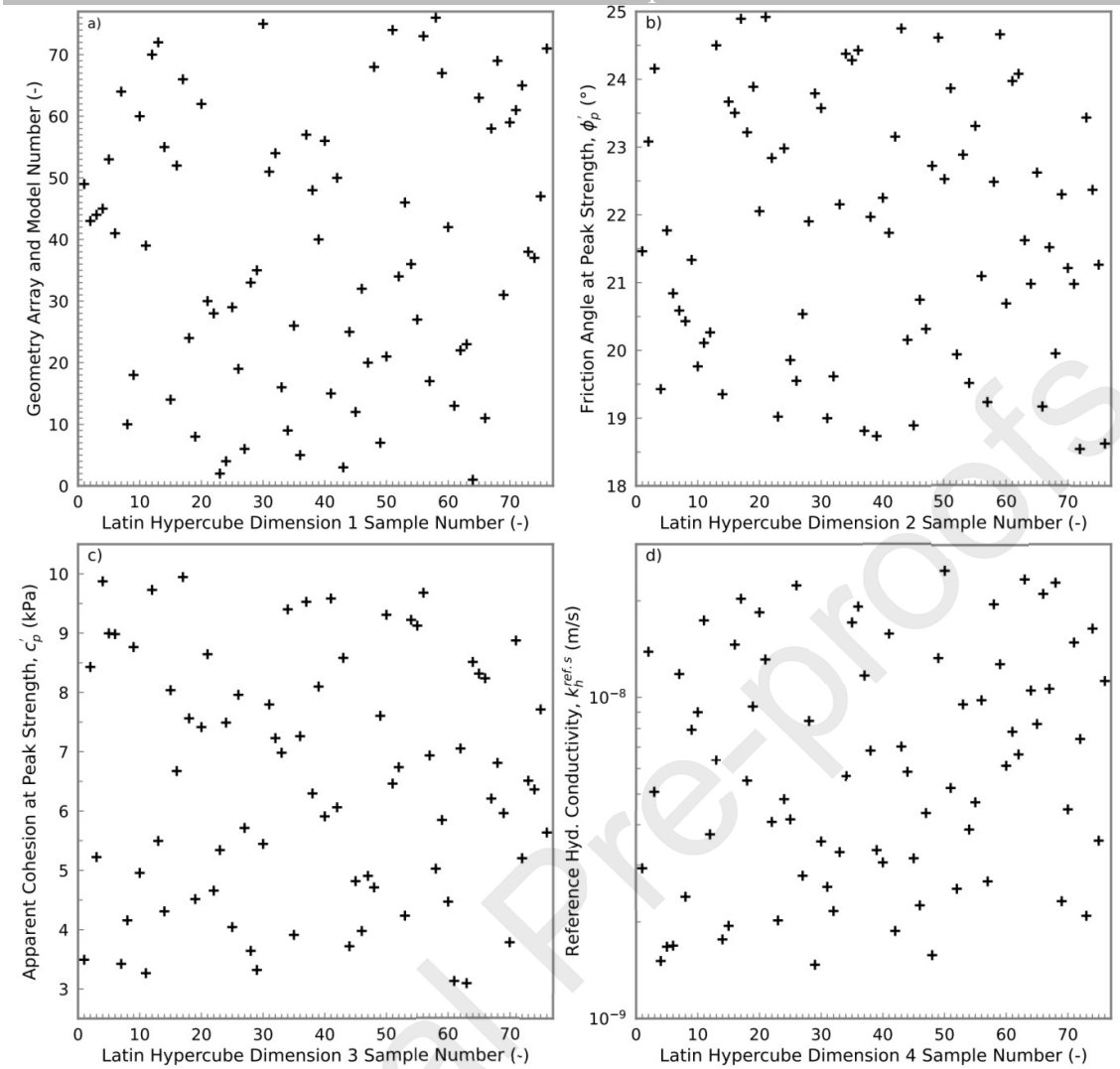

Figure 2: Latin hypercube design dimension vectors showing the samples for a) the model geometry number (see Figure 8); b) the peak frictional strength; c) the apparent cohesion at peak strength and d) the reference hydraulic conductivity value. The values are obtained on a unit interval [0,1] and are then scaled to the required range.

2.2 Geotechnical deterministic modeling overview

In order to develop the emulator, it is necessary to undertake deterministic numerical modeling of the assets of interest, and the resultant data can then be used to train the emulator. In this work, the deterioration of infrastructure cut, and embankment slopes are the focus. This required the development of two differing models to capture the fundamentally different initial stress conditions in the soil forming the slopes as a result of the differing construction methods.

In cut slopes, a key aspect of deterioration is driven by the long-term dissipation of construction induced negative pore pressures, which, along with the overconsolidated nature of the clays of interest, can cause loss of strength due to effective stress changes. This, in turn, can also cause strength reduction due to shear strain softening driven by swelling and seasonal ratcheting. Conversely, the embankments are at greatest risk of deep-seated failure during and shortly after construction due to loading generating excess positive pore pressures in the foundation soils. Once these initial excess positive pore pressures dissipate, the average stability of embankments increases, and shallow failures driven by seasonal weather cycles become more

significant. In addition, the compaction process of fill layers during construction, even using modern methods, can introduce heterogeneity of density into the structure of the embankment as well as a complex stress and stiffness distribution which influences later behavior [2]. These processes are summarized in Figure 3a and b where the key mechanisms for each asset type are highlighted.

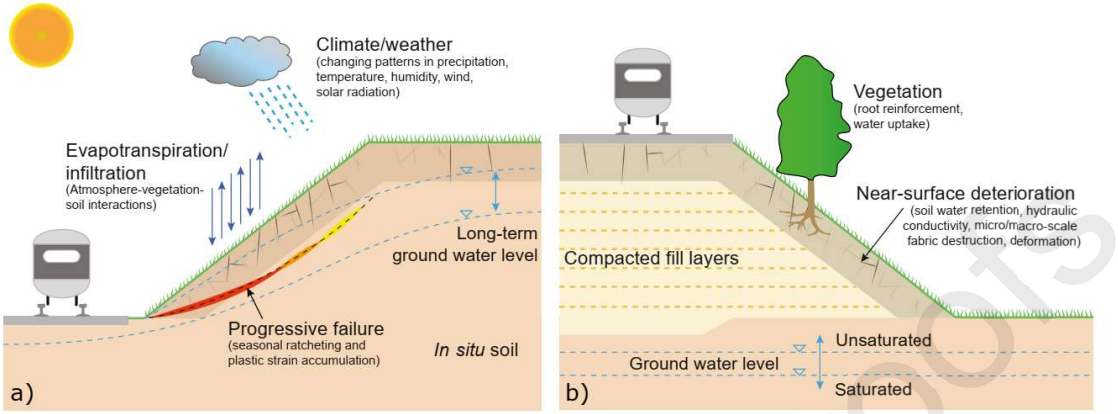

Figure 3: Conceptual slope processes and behavior modeled in this work; a) cut slopes; b) embankment slopes.

3 Deterministic geotechnical model development

The modeling in this work is undertaken in the software code FLAC (Fast Lagrangian Analysis of Continua), a finite-difference geomechanics modeling code intended for use in rock and soil mechanics problems [27] and referred to as the deterministic geotechnical model (DGM) in the remainder of the text. Within the DGM, the model is discretized into deformable zones in order to solve a set of differential equations governing soil hydraulic and mechanical behaviors. Stresses, strains, and displacements for discrete points are then calculated. Deformations occur within the model as a function of the stress-strain relationship adopted and as a result of applied boundary conditions. The DGM finds a static solution to an unstable physical problem using an explicit, time stepping approach. Additionally, the DGM has the capability to model fluid flow. This is carried out as coupled consolidation analysis, whereby deformations drive changes in pore pressure, and vice-versa. In this work the two-phase flow scheme was adopted, which was capable of modeling unsaturated flow where air and liquid phases are considered within a permeable medium. This allowed the modeling of the coupled hydromechanical behavior of both cuttings and embankments.

3.1 Saturated hydraulic conductivity

The saturated hydraulic conductivity, k_h, of the cut slope models is defined as a function of the depth below the modeled surface, d_s, prior to slope excavation and is derived from published data on the London Clay [28,29]. The model also incorporates a near-surface weathered zone of elevated conductivity. The initial k_h distribution prior to slope excavation is derived as follows:

$$k_h = k_h^{ref}\left(d_s^{\,k_h^{scale}}\right) \text{where} \begin{cases} k_h^{scale} = -0.8,\ k_h^{ref} = 1 \times 10^{-8}\ \text{m/s, if } d_s \le 5\ \text{m} \\ k_h^{scale} = -1.0,\ k_h^{ref} = 2 \times 10^{-9}\ \text{m/s, if } d_s > 5\ \text{m,} \end{cases} \quad (1)$$

where k_h^{ref} represents the saturated hydraulic conductivity of the soil at a reference depth of 1 m, and k_h^{scale} controls the rate of change of saturated conductivity with depth. Also note that the maximum near surface hydraulic conductivity is capped at 1×10^{-7}m/s.

Field measurements of the near-surface hydraulic conductivity of a cut slope in London Clay indicate an elevated hydraulic conductivity in the weathered zone within the top 4 m of material below the excavated slope surface [30]. To approximate this behavior, a high conductivity zone was defined in the cutting models at the end of excavation, where the saturated hydraulic conductivity below the excavated surface, d_s^n, is defined as follows:

$$k_h = \begin{cases} k_h^{ref}\left(d_s^{n\,-0.8}\right),\ k_h^{ref} = k_{hs}^{ref}, \text{ if } d_s^n \le 4 \text{ m} \\ \text{unchanged from previous, if } d_s^n > 4 \text{ m,} \end{cases} \quad (2)$$

where k_{hs}^{ref} is the weathered soil reference saturated hydraulic conductivity at a depth of 1 m. The hydraulic conductivity properties adopted for the cut slope validation model are summarized in Table 1.

The embankment simulations use a void ratio dependent model for the hydraulic conductivity of the fill, k_{hf}, according to the formula proposed by Samarasinghe *et al.* [31]:

$$k_{hf} = k_{hf}^{ref}\left(\frac{e^{k_{hf}^{l}}}{1+e}\right) \quad (3)$$

where k_{hf}^{ref} is the reference hydraulic conductivity ($k_{hf}^{ref} = 1 \times 10^{-6}$ m/s) and k_h^l is a fitting parameter ($k_h^l = 5$). The fill hydraulic conductivity was calibrated from the field data reported by Dixon *et al.* [30] for the BIONICS trial embankment. The adopted hydraulic conductivity properties for the embankment validation model are summarized in Table 2.

3.2 Soil water retention and unsaturated hydraulic conductivity

Both the cut slope and embankment models use the van Genuchten [32] soil water retention model to link the degree of saturation, S_w, and the capillary pressure, P_c when the soil becomes unsaturated, derived as follows:

$$P_c = P_{vg}\left[S_e^{-1/m_{vg}} - 1\right]^{1-m_{vg}} \quad (4)$$

Where P_{vg} is a fitting parameter related to the air entry value of the material, m_{vg} controls the rate at which the material desaturates once air entry has occurred and S_e is the effective saturation:

$$S_e = \frac{S_w - S_{wr}}{1 - S_{wr}} = \frac{\theta - \theta_r}{\theta_s - \theta_r} \quad (5)$$

Where S_{wr} is the residual wetting saturation, θ is the volumetric water content, θ_r is the residual volumetric water content and θ_s is the saturated volumetric water content (equal to the porosity of the soil).

The models also derive the unsaturated hydraulic conductivity, k_{uh}, and the unsaturated air conductivity, k_{ua}, from S_e as follows:

$$k_{uh} = k_h S_e^{0.5}\left[1 - \left(1 - S_e^{1/m_{vg}}\right)^{m_{vg}}\right]^2 \quad (6)$$

$$k_{ua} = k_h \frac{\mu_w}{\mu_a}(1 - S_e)^{0.5}\left(1 - S_e^{1/m_{vg}}\right)^{2m_{vg}} \quad (7)$$

Where μ_w/μ_a is the water-to-air dynamic viscosity ratio.

The adopted soil water retention behavior for the cut slope model was calibrated against published soil water retention drying curve data for London Clay [33]. The adopted soil water retention behavior for the fill validation models was bimodal and had variable porosity as a function of volume change [see 34].

3.3 Soil stiffness

Both the cutting and embankment models adopt non-linear stress-dependent stiffness models. In the cut slope models, soil elastic modulus, E', is defined as a function of mean stress, p', and a constant Poisson's ratio, υ. This approach is widely adopted [35–39]. E' is derived as follows:

$$E' = \frac{E'_0(p' + 100)}{100} \quad (8)$$

Where E'_0 is the reference modulus of elasticity and p' is derived from the cartesian effective stresses as follows: $p' = (\sigma'_{xx} + \sigma'_{yy} + \sigma'_{zz})/3$. The adopted cut slope stiffness parameters are summarized in Table 1.

Stress-dependent elastic modulus and Poisson's ratio functions were used to define the stiffness of the embankment slope models, as follows:

$$E' = E'_0\left(\frac{p'}{p_0}\right)^{p_e} \quad (9)$$

$$\upsilon = -p_\upsilon ln\left(\frac{p'}{p_0}\right) + \upsilon_0 \quad (10)$$

This approach has previously been adopted for embankment models [e.g. 34,40]. Where E_0 is the reference elastic modulus at p' of 1 atm, υ_0 is the reference Poisson's ratio at p' of 1 atm, p_e is the elastic modulus stress

exponent, p_v is the Poisson's ratio stress parameter, and p_0 is the reference stress (1 atm). The adopted values are summarized in Table 2.

3.4 Conceptual shear strength behavior of clays

At relatively low effective stresses such as those in cutting and embankment slopes, overconsolidated clays typically exhibit peak strengths caused by soil structure [41,42] and also due to their relative density, whereby their void ratio being lower than the critical state void ratio, allows dilation to occur during shearing, with the dilation angle reaching a peak, corresponding to the peak strength of the material. As the void ratio of the dilating material continues to increase and approach the critical void ratio, dilation decreases and the strength reduces beyond peak, until the void ratio reaches the critical value and strains can occur at constant volume and at constant shear stress (the critical state strength, ϕ_{cs}).

In order to simulate the shear strength and strain softening behavior described above, the cutting and embankment models take differing approaches to account for the different nature of their formation. In the cutting model, the peak strength behavior of the overconsolidated clay, as caused by dilation during shearing, is simulated using an apparent cohesion via a non-zero cohesion intercept for the Mohr-Coulomb envelope, rather than through adoption of a non-zero dilation angle. The critical state friction angle is adopted for peak. The linear nature of the Mohr-Coulomb envelope also does not capture the suppression of dilation at higher stresses or the curvature of the strength envelope at low confining stresses.

The post-peak strength reduction towards critical state strength due to decreasing dilation of the soil is simulated by decreasing the apparent cohesion intercept to zero with increasing plastic shear strains, while maintaining the frictional strength at the critical state value. The strength parameters adopted for the high plasticity clay used in the cut slope models are summarized in Table 1.

The embankment model adopts a different approach to simulating the peak strength behavior, in part due to the requirement to simulate compaction effects during construction and a more gradual transition from elastic to plastic behavior. Rather than simulating the peak strength behavior purely by use of a peak apparent cohesion intercept, it makes use of a constant apparent cohesion in the peak strength region, and an initial strain hardening mechanism with gradually increasing friction and dilation angles to mobilize the peak strength under shearing due to dilation. As strains pass peak and approach the post peak value, the dilation angle reduces to simulate the reduction in dilation as the void ratio of the material more closely approaches the critical void ratio. Further increases in shear strain beyond the post peak value lead to a continuing reduction in the dilation angle and also result in the apparent cohesion intercept and frictional component of strength reducing to their critical state values. The model also includes a time dependent change in the peak strength values to simulate the non-shear driven softening down to the normally consolidated peak strength as described by Skempton [43]. The strength parameters adopted for an intermediate plasticity clay (a glacial till) used in the embankment slope validation model are summarized in Table 2.

At large shear strains beyond the critical state, significant soil particle re-orientation and alignment can occur [44], which leads to an additional reduction in shear strength due to changes in the friction angle of the material as seen in both ring shear and reversal shear tests [44,45]. This behavior is represented in both the

embankment and cutting models by a reduction in the friction angle of the soil from the critical state strength to a minimum value representing the residual strength with increasing magnitudes of plastic shear strains.

Due to the strain softening model employed in this work, the transition from continuum strain to deformation concentrated along a slip surface can be captured. It should be noted that although modeling of propagating displacement discontinuities to represent strain localization has not been implemented in the adopted numerical framework, the related issue of mesh dependency has been reduced through the use of a nonlocal regularization approach [36,46–49]. In addition, the strains mobilized by the failed mass are not significant enough to require alternative methods more suitable for large strains, such as the discrete element or material point methods, which are typically employed in situations involving debris flows, landslide runout, or other problems characterized by very large strains.

The adopted approach, with the potential for softening to a large displacement residual strength, replicates the strength reduction mechanisms discussed by Leroueil [50] which allows for localized sections of a nominal shear surface to soften at different rates, with some portions approaching residual while others remain at some post-peak or even peak strength. This behavior has been observed in the field [51] and is also discussed in the context of first time failures whereby the average shear strength on the failure surface may be equivalent to the normally consolidated peak strength, but localized parts of the shear surface may reach residual [see the discussion in 51–53]. The strength behavior for the cut slope and embankment models is summarized in schematic form in Figure 4.

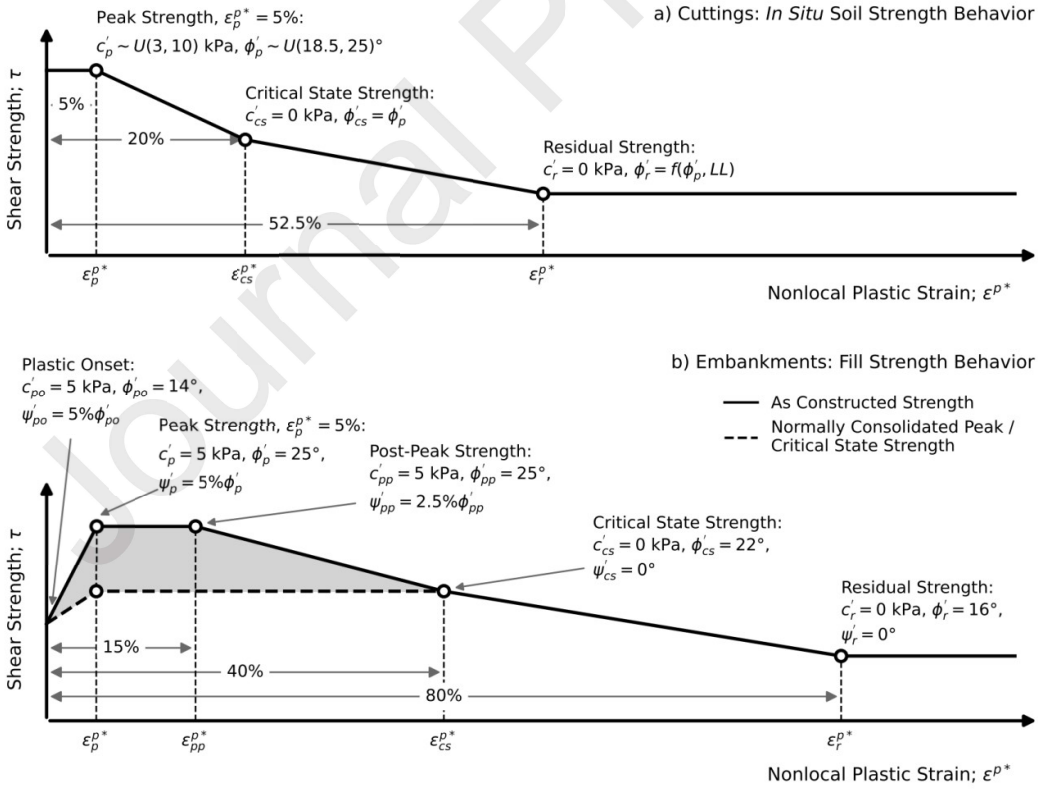

Figure 4: Schematic strain softening behavior. a) cut slope models of natural overconsolidated high plasticity clay as used to produce emulator input data where the residual strength, ϕ'_r, is a function of the peak strength and assumed liquid limit $f(\phi'_p, LL)$; b)

intermediate plasticity compacted clay fill with time dependent softening from the peak value to the normally consolidated peak strength / critical state value. The material properties are summarized in Table 1 and Table 2.

3.5 Mohr-Coulomb strain softening model

The adopted constitutive model for both the cutting and embankment slopes is a Mohr-Coulomb strain softening model where the shear strength properties (friction angle, ϕ', apparent cohesion, c', and dilation angle, ψ') are made a variable function of the plastic shear strain, ε^p, derived as follows:

$$\Delta\varepsilon^p = \sqrt{\frac{1}{2}\left(\Delta\varepsilon^{p1} - \Delta\varepsilon^{pm}\right)^2 + \frac{1}{2}\left(\Delta\varepsilon^{pm}\right)^2 + \frac{1}{2}\left(\Delta\varepsilon^{p3} - \Delta\varepsilon^{pm}\right)^2} \quad (11)$$

where $\Delta\varepsilon^{p1}$ and $\Delta\varepsilon^{p3}$ are the major and minor principal plastic strains and $\Delta\varepsilon^{pm} = \left(\Delta\varepsilon^{p1} + \Delta\varepsilon^{p3}\right)/3$.

In order to reduce the mesh dependency of the solution, a nonlocal softening approach [46] is adopted utilizing the weighting function, ω, proposed by Galavi and Schweiger [47]. This approach introduces an additional softening parameter, the internal length, l_i, that controls the relative contribution of neighboring zones to the averaged nonlocal plastic shear strain, $\varepsilon^{p\,*}$. Nonlocal plastic shear strain is calculated for a given zone, $\varepsilon_z^{p\,*}$, by averaging the plastic strains from neighboring zones as follows:

$$\varepsilon_z^{p\,*} = \frac{1}{A_w}\sum_{z_n=1}^{z_t} \omega_{z_n}\varepsilon_{z_n}^p A_{z_n} \quad (12)$$

where z_n is the finite difference grid zone number of a zone neighbouring z, z_t is the total number of zones within the radius of influence ($r_i \cong 3l_i$), ω_{z_n} is the weighting function calculated for z_n, A_{z_n} is the area of z_n and A_w is the sum of weighted zone areas:

$$A_w = \sum_{z_n=1}^{z_t} \omega_{z_n} A_{z_n} \quad (13)$$

The weighting function is derived from l_i as follows:

$$\omega(r) = \frac{r}{l_i^2}^{-\left(\frac{r}{l_i}\right)^2} \quad (14)$$

where r is the distance between zone, z, for which nonlocal softening is being derived and neighboring zone, z_n, within r_i.

In addition to plastic shear strain softening, the embankment model introduces a strength dependency on the number of annual cycles experienced by the fill, N_s. This approximates the reduction of the overconsolidated peak strength parameters (c'_p, ϕ'_p, ψ'_p) to the normally consolidated value as per Skempton [43]. The shear strength reduction due to seasonal cycles is derived as follows:

$$\tau_{red} = (\tau_p - \tau_{nc})e^{\xi N_s} + \tau_{nc} \quad (15)$$

Where τ_{red} is the reduced shear strength parameter, τ_p is the shear strength parameter at peak, τ_{nc} is the reduced normally consolidated strength parameter value, and ξ is the shear strength decay parameter. For full details of this behavior and the derivation of the material parameters, see Morsy et al. [34].

Table 1: Mechanical and hydrological parameters for the overconsolidated high plasticity clays simulated in the cut slope models used for training the Gaussian process emulator.

Parameter	Symbol	Units	Value
General Properties			
Dry density	ρ_d	kg/m^3	1550
Hydrological Properties			
Near surface reference hydraulic conductivity* (≤5 m below model surface)	k_{hs}^{ref}	m/s	$\frac{(2.50 \times 10^{-8})^X}{(1.45 \times 10^{-9})^{X-1}}$
Reference hydraulic conductivity at depth (>5 m below model surface)	k_{hd}^{ref}	m/s	2.00×10^{-9}
Hydraulic conductivity at near surface depth, d	k_{hs}	m/s	$k_{hs}^{\text{ref}} d^{-0.8}$
Hydraulic conductivity at depth, d	k_{hd}	m/s	$k_{hd}^{\text{ref}} d^{-1}$
Van Genuchten fitting parameter	p_0	kPa	62.5 (weathered clay) 125.0 (unweathered clay)
Van Genuchten fitting parameter	n_{vg}	-	1.18
Van Genuchten fitting parameter	m_{vg}	-	$1 - 1/n_{vg} \cong 0.153$
Saturated volumetric water content	θ_s	-	0.45
Residual volumetric water content	θ_r	-	0.10
Mechanical Properties			
Reference modulus of elasticity	E'_0	kPa	5000.0

Modulus of elasticity	E'	kPa	$E' = \frac{E'_0(p' + 100)}{100}$
Poisson's ratio	υ	-	0.2
Nonlocal plastic shear strain at peak strength	$\varepsilon_p^{ps\,*}$	%	5.0
Nonlocal plastic shear strain at critical state strength	$\varepsilon_{cs}^{ps\,*}$	%	20.0
Nonlocal plastic shear strain at residual strength	$\varepsilon_r^{ps\,*}$	%	52.5
Nonlocal internal length	l_i	m	1.0
Friction angle at peak strength	ϕ'_p	°	$\phi'_p \sim U(18.5,25.0)$
Friction angle at critical state strength	ϕ'_{cs}	°	$\phi'_{cs} = \phi'_p$
Friction angle at residual strength	ϕ'_r	°	7.5 to 16. See section 5.2.
Cohesion at peak strength	c'_p	kPa	$c'_p \sim U(3,10)$
Cohesion at critical state strength	c'_{cs}	kPa	0.0
Cohesion at residual strength	c'_r	kPa	0.0
Dilation angle	ψ'	°	0.0

* X in the reference conductivity is the Latin hypercube sample value

Table 2: Mechanical and hydrological parameters for the intermediate plasticity clay fill simulated in the embankment model (Morsy et al. 2023).

Parameter	Symbol	Units	Value
General Properties			
Bulk density	ρ_b	kg/m^3	2018
Hydrological Properties			
Reference hydraulic conductivity	k_h^{ref}	m/s	1.00×10^{-6}
Hydraulic conductivity	k_h	m/s	$k_h = k_h^{\text{ref}}\left(e^5/1 + e\right)$
Van Genuchten fitting parameter	p_{vg}	kPa	80.0
Van Genuchten fitting parameter	n_{vg}	-	$n_{vg} = 1/(1 - m_{vg}) \cong 1.333$
Van Genuchten fitting parameter	m_{vg}	-	0.25
Saturated volumetric water content	θ_s	-	0.36
Residual volumetric water content	θ_r	-	0.00
Mechanical Properties			
Reference modulus of elasticity	E_0	-	360.0
Modulus of elasticity	E'/p_0	-	$E'/p_0 = E_0\left(p'/p_0\right)^{p_e}$
Mod. of elasticity stress exponent	p_e	-	0.25
Reference Poisson's ratio	υ_0	-	0.20
Poisson's ratio	υ	-	$\upsilon = -p_\upsilon ln\left(p'/p_0\right) + \upsilon_0$

Poisson's ratio fitting parameter	p_v	-	0.05	
Nonlocal internal length	l_i	m	1.0	
Nonlocal peak plastic shear strain	ε_p^{ps*}	%	5.0	
Nonlocal post-peak plastic shear strain	ε_{pp}^{ps*}	%	15.0	
Nonlocal critical state plastic shear strain	ε_{cs}^{ps*}	%	40.0	
Nonlocal residual plastic shear strain	ε_r^{ps*}	%	80.0	
Strength decay parameter	ξ	-	− 0.1	

			As placed strength	**Strength at >30 years**
Friction angle at plastic onset	ϕ'_{po}	°	14.0	14.0
Friction angle at peak strength	ϕ'_p	°	26.0	22.0
Friction angle at end of peak	ϕ'_{pp}	°	26.0	22.0
Friction angle at critical state strength[A]	ϕ'_{cs}	°	22.0	22.0
Friction angle at residual strength	ϕ'_r	°	16.0	16.0
Cohesion at plastic onset	c'_{po}	kPa	5.0	0.0
Cohesion at peak strength	c'_p	kPa	5.0	0.0
Cohesion at end of peak	c'_{pp}	kPa	5.0	0.0
Cohesion at critical state strength[A]	c'_{cs}	kPa	0.0	0.0

Cohesion at residual strength	c'_r	kPa	0.0	0.0
Dilation angle at plastic onset	ψ'_{po}	°	5.0% of ϕ'_{po}	0.0
Dilation angle at peak strength	ψ'_p	°	5.0% of ϕ'_p	0.0
Dilation angle at end of peak	ψ'_{pp}	°	2.5% of ϕ'_p	0.0
Dilation angle at critical state strength	ψ'_{cs}	°	0.0	0.0
Dilation angle at residual strength	ψ'_r	°	0.0	0.0

[A]The critical state strength can be reached by either plastic shear strain softening, a time dependent decay in strength or some combination of both.

4 Deterministic geotechnical model validation

In this section, the validation of the cutting and embankment slopes is summarized.

4.1 Cut slope model validation

The stiffness and strength properties of the cut slope model were calibrated against oedometer swelling data [29,54] and constant vertical stress, simple shear tests [55] on samples of the London Clay. The results of the stiffness and strength calibration are summarized in Figure 5.

Figure 5a shows that the adopted stiffness produces swelling behavior that compares well with that of London Clay. Figure 5b shows the calibration of the adopted coefficient of at-rest lateral earth pressure, K_0, and indicates that a K_0 of 1.5 delivers the closest approximation to the laboratory response. Figure 5c presents the laboratory and modeled stress-strain behavior. The model simulations are in overall good agreement with the experimental data. Figure 5d shows the calibration of the nonlocal internal length parameter and demonstrates the reduction in mesh dependency of the nonlocal versus local strain softening models [36].

Hydrological validation was undertaken by comparing pore water pressure time histories from cut slope modeling to data from an instrumented highway cutting excavated in overconsolidated high plasticity clay [56,57]. This comparison can be seen in Figure 6. The full details of the calibration and validation modeling are given in Rouainia et al. [38] and Postill et al. [36]. The ability of the cut slope modeling approach to replicate seasonal ratchetting behavior was validated against centrifuge test data and is available in Postill et al. [58].

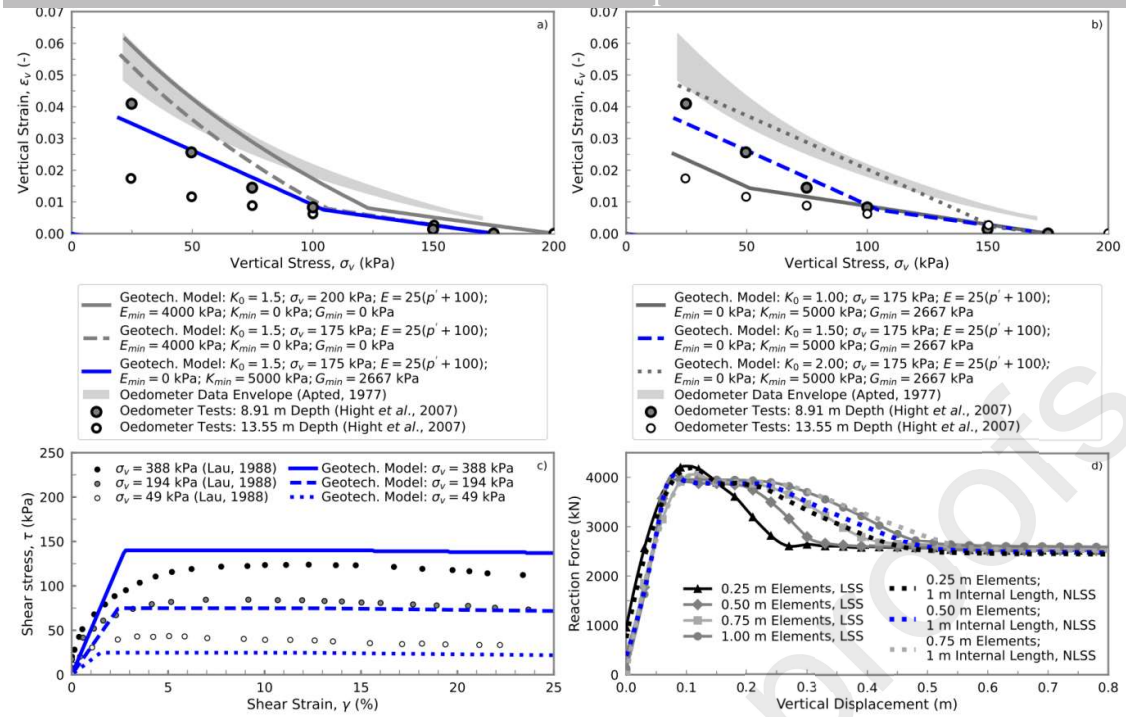

Figure 5: a) & b) Calibration of the stiffness model [36] against oedometer swelling data at differing assumed values of K_0 [29,54]; c) Constant vertical stress, simple shear test data for London Clay [55] compared to the deterministic geotechnical model adopting local strain softening (LSS); d) Biaxial test data model used to calibrate the nonlocal strain softening (NLSS) model [after 36]. Adopted parameters highlighted in blue.

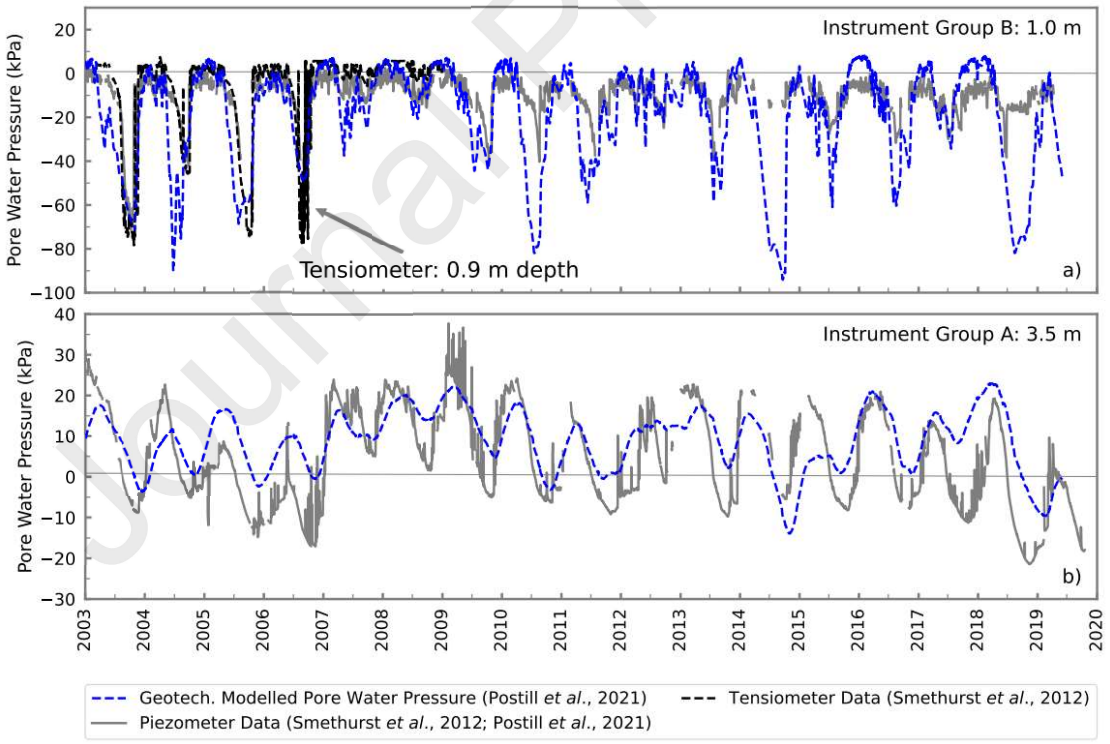

Figure 6: Validation of modeled cut slope hydrological behavior [36] against field tensiometer and piezometer data [56,57]; a) near surface behavior in the weathered London Clay; b) pore pressure cycles at greater depth in the lower permeability London Clay.

4.2 Embankment slope model validation

The embankment stiffness and strength models were calibrated against data from consolidated-undrained triaxial tests with pore water pressure measurements on an intermediate plasticity soil used as a fill in an instrumented trial embankment, known as the BIONICS research embankment [1,59,60]. The element scale model and laboratory stress-strain curves for the fill and foundation material are shown in Figure 7a and Figure 7b where it can be seen that the pre- and post-peak stress-strain behavior is accurately replicated by the adopted model and model properties. The resultant pore pressure generation due to the undrained nature of the response is shown in Figure 7c and Figure 7d where the pore pressure response of the fill is reasonably well captured, and the dilatant nature of the overconsolidated material in the embankment foundation, which generates negative pore pressures during shearing is very effectively captured by the model. The embankment construction modeling approach was validated by comparing modeled deformations against published deformation data [61]. The comparison of modeled and published horizontal and vertical displacements can be seen in Figure 7e and Figure 7f. For full details of the embankment modeling framework see [34].

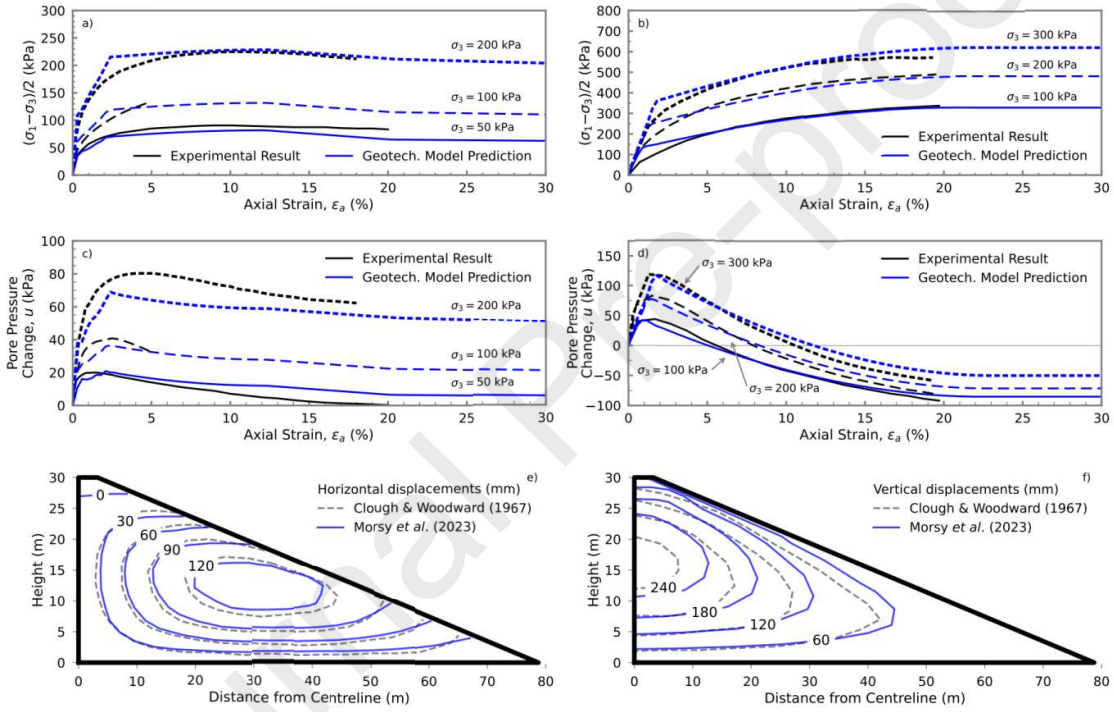

Figure 7: Validation of the embankment model; a) and c) modeled and laboratory undrained triaxial test data for the BIONICS embankment fill [after 34]; b) and d) modeled and laboratory undrained triaxial test data for the BIONICS embankment foundation soil [after 34]. e) and f) comparison of displacements derived using the current modeling approach to published vertical and horizontal displacements within an embankment [61].

5 Experimental design, parameter selection and parameter scaling

The validated cut and embankment slope models described previously serve as the baseline for the parametric study used to produce the input data that trained the emulator. In this work the derivation of the data for the cut slope models and their emulation is summarized. Previous modeling work has identified that cut slope stability, deterioration and time to failure is sensitive to the slope geometry [height and angle, see: 35,37,62], shear strength parameters [35,63], and soil hydraulic conductivity [38]. Accordingly, parameters defining slope geometry, shear strength, and soil hydraulic conductivity were selected as variables in the experimental design of the deterministic model simulations.

5.1 Slope geometry adopted in emulator models

To define practical ranges of cut slope geometries (slope heights and angles), data were derived from two sources: (1) LiDAR surveys of the slopes along the UK Great Western Main Line (GWML) between London and Bristol; and (2) walk-over survey data from the UK M4 motorway between London and Bristol. The data were provided by project stakeholders (National Highways, Network Rail, and Mott MacDonald). Figure 8 presents the processed data and the geometries that were used in the experimental design, where it can be seen that the typical height of highways cuts and their maximum slope angle is typically lower than that for the rail cuttings.

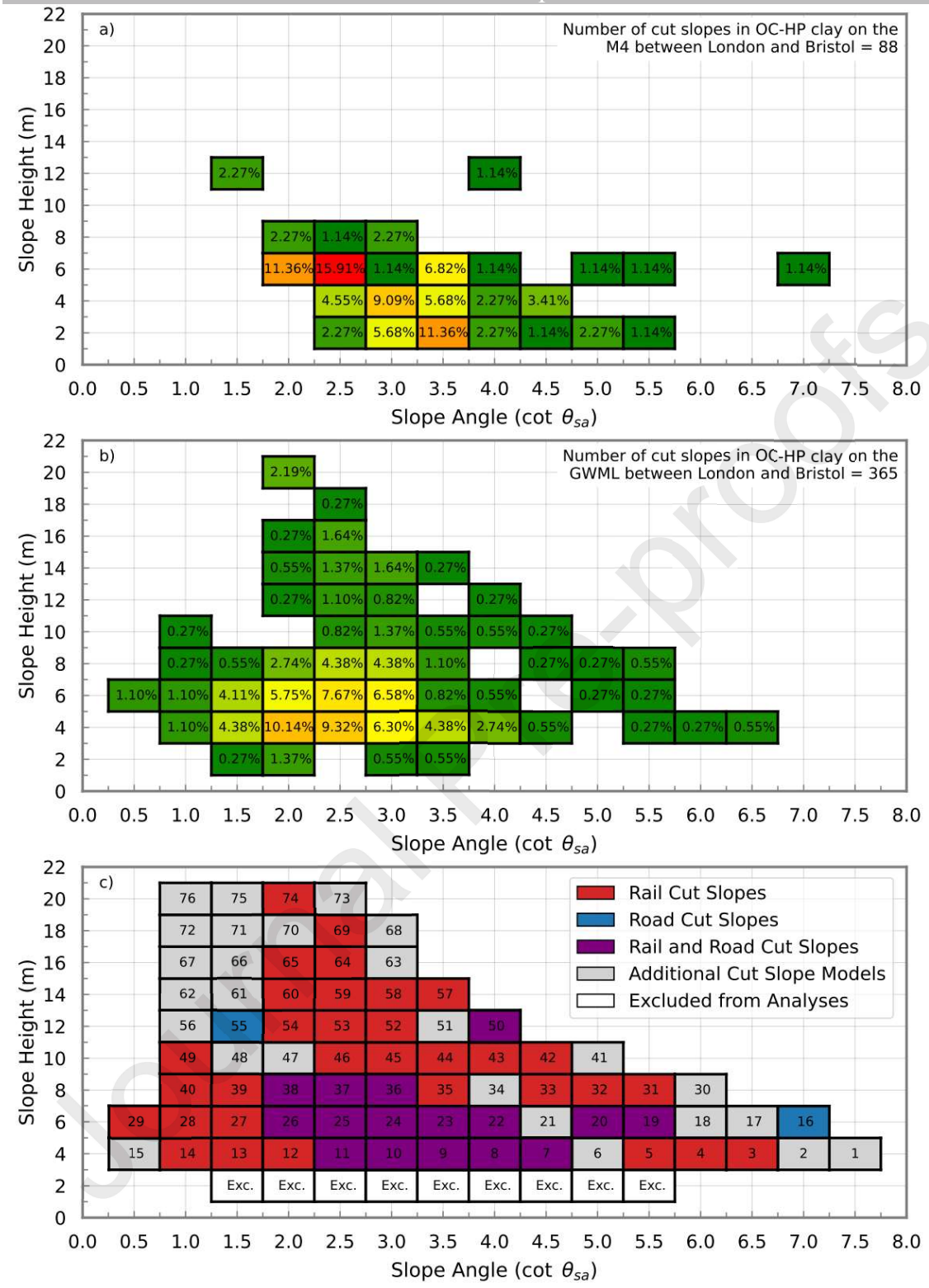

Figure 8: Percentage of cut slopes of varying geometries excavated into overconsolidated high plasticity (OC-HP) clays on a) the M4 motorway and b) the Great Western Main Line (GWML) railway between London and Bristol; c) the finalized geometry array from the experimental design showing the model numbers [after 64]. Slopes less than 3 m tall were excluded from the analyses.

5.2 Material strength adopted in emulator models

The range of adopted shear strength and hydraulic conductivity parameters for the overconsolidated high plasticity (OC-HP) clays were derived from previous modeling studies [35,37,65] and published laboratory and field data [29,54,55,66–73].

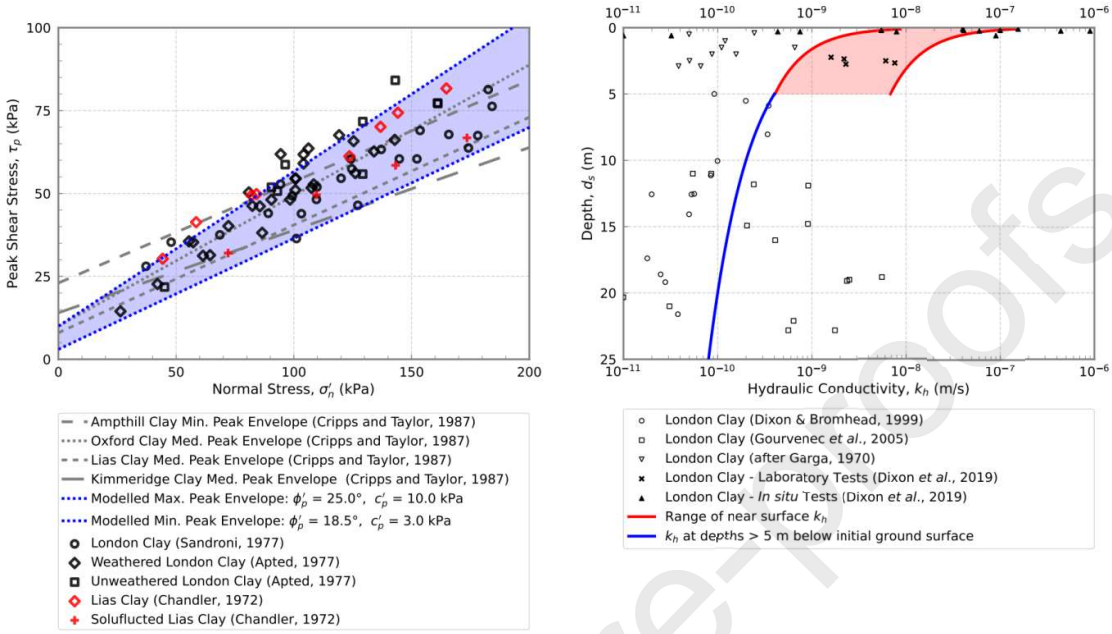

Figure 9: a) Adopted peak strength envelope range for the modeling of overconsolidated high plasticity (OC-HP) clays; b) adopted hydraulic conductivity range and variation with depth.

The range of adopted peak strength envelopes is shown in Figure 9a, overlain on literature data of peak shear strength for overconsolidated clays with similar (high) plasticity. A number of which are also found on the route of the M4 motorway and GWML railway. Based on these data, the peak shear strength parameters for the models (c'_p, ϕ'_p) were assumed to be uncorrelated, random, uniformly distributed variables as follows, $c'_p \sim U(c'_{p\,min}, c'_{p\,max})$; $\phi'_p \sim U(\phi'_{p\,min}, \phi'_{p\,max})$, where $c'_{p\,min} =$ 3 kPa; $c'_{p\,max} =$ 10 kPa, $\phi'_{p\,min}$= 18.5° and $\phi'_{p\,max} =$ 25° (where the subscripts min and max denote minimum and maximum values of the selected parameter ranges).

In this work, for cutting slopes it is assumed that the change in strength from peak to critical state strength is due to the halting of dilatant behaviour, simulated here as an apparent cohesion intercept that falls to zero. As such the peak and critical state friction angles are assumed to be equal.

The value of the residual friction angle was determined by the plasticity-strength relationships outlined in Stark *et al*. [74], where the change in friction angle from the fully softened value [which approximates critical state, 43] to the residual value, is a function of the liquid limit, LL, the clay fraction, CF, of the soil ($CF \geq 50\%$) and the assumed *in situ* stress range (50 to 100 kPa).

The data from Stark *et al*. [74] were used to estimate the LL from the peak friction angle range derived from the literature for London Clay (see Figure 9a), and then those LL values were used to estimate the reduction

in frictional strength to the residual value while constraining the range to not exceed the residual strength seen in the literature (see Figure 10).

The resultant residual strength envelopes are plotted against field and laboratory data [44,75,76] along with values previously adopted in the modeling of OC-HP clays [35,37,65,77] in Figure 10, where it can be seen that the adopted values capture the majority of the range of observed residual strengths, with the exception of the extremes which are a function of atypical mineralogy or particle size distribution and are highlighted in the figure.

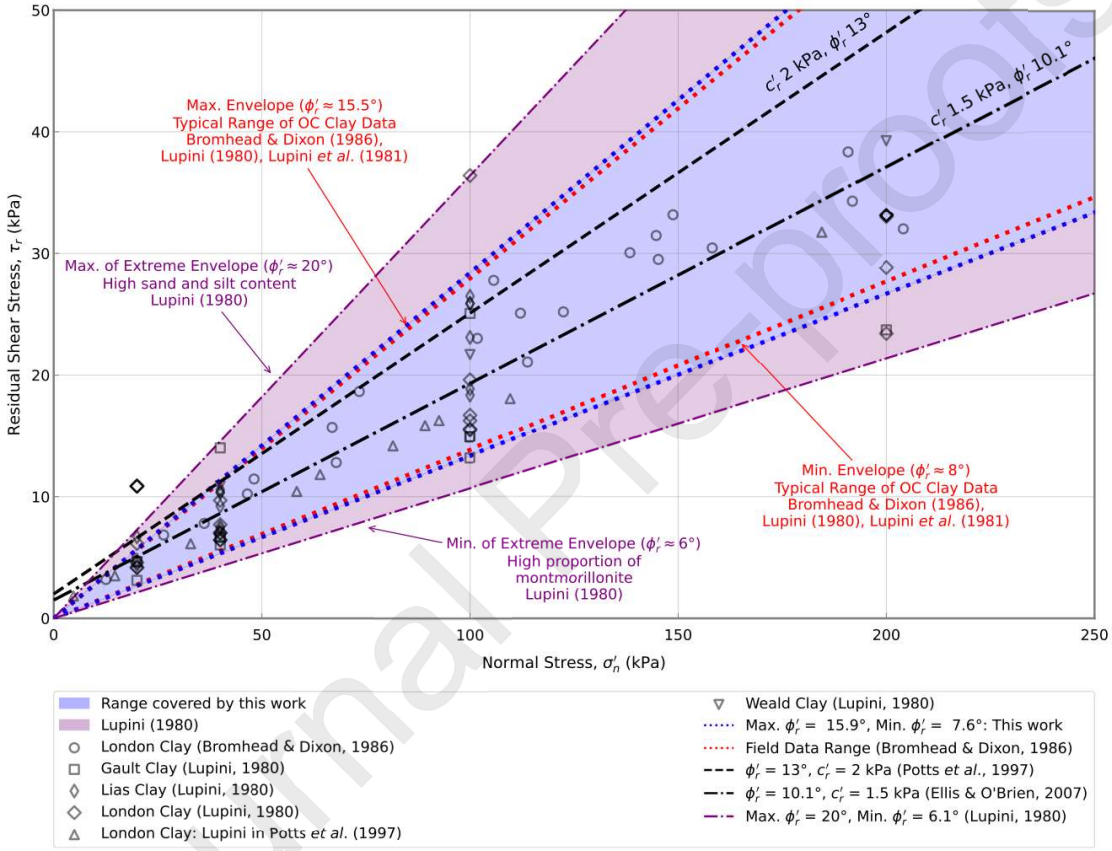

Figure 10: The residual frictional strength range adopted in the modeling compared to laboratory and field data along with the residual strength adopted for overconsolidated high plasticity clays in other work.

5.3 Hydraulic conductivity adopted in the emulator training models

The hydraulic conductivity parameter refers to the near surface reference conductivity, k_{hs}^{ref} (m/s) used in the DGM cut slope model to calculate the hydraulic conductivity (k_h) at increasing depth below the initial and excavated ground surface, where k_{hs}^{ref} is derived from a sample (X) of the LHS hydraulic conductivity vector as follows:

$$k_{hs}^{ref} = \frac{\left(k_{hs}^{max}\right)^X}{\left(k_{hs}^{min}\right)^{X-1}} \quad (16)$$

where k_{hs}^{max} and k_{hs}^{min} are the maximum and minimum values of the selected range of k_{hs}^{ref}. The range of near surface hydraulic conductivity and the adopted hydraulic conductivity profile at depth is summarized in Figure 9b.

5.4 Summary of key outcomes from the geotechnical modeling

Figure 11 illustrates a series of deterioration curves, that are direct outputs of the deterministic geotechnical models, showing the reduction in FoS with increasing time. From Figure 11 a number of trends can be ascertained, whereby it appears that the time to failure (i.e., *FoS* = 1) is correlated to the slope height and the adopted shear strength parameters, however it is unclear exactly what relative effect the individual parameters have on the time to failure. This is further complicated by the 14 m high slope model which has a significantly different response due to the difference in adopted strength and hydraulic conductivity properties. This helps to illustrate that the deterministic geotechnical model outputs from the LHS experimental design are not meant to be interpreted directly, but instead require emulation.

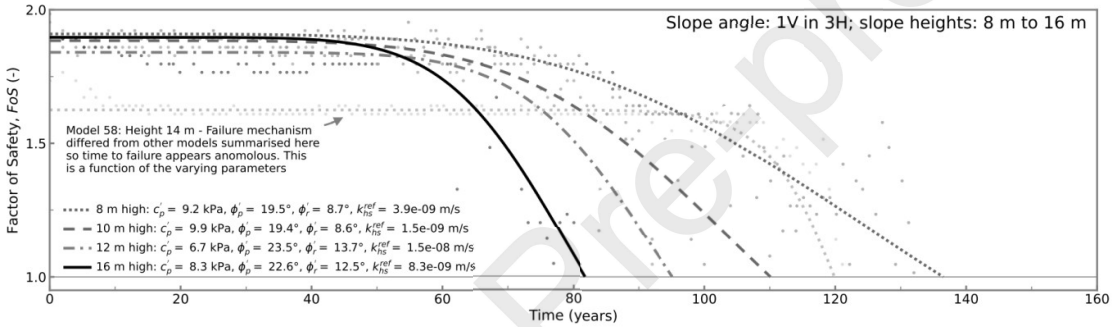

Figure 11: Example factor of safety deterioration curves for a range of geometries and material parameters derived from the deterministic geotechnical models which used the Latin hypercube experimental design input parameters.

6 Statistical emulator

Deterministic models, such as the ones presented in Sections 4.1 and 4.2 (the DGM), are an effective tool to simulate earthwork deterioration. However, a typical run of the DGM can take from 2 days up to 30 days to execute, depending on the adopted model mesh and the fluid flow time step (a function of zone size and hydraulic conductivity). Although individual model runs can be used to understand deterioration for a prescribed set of material properties and boundary conditions, it is impractical to run the number of DGM simulations that would be required to understand the continuous relationships between multivariate inputs (e.g. earthwork geometry and soil properties) and outputs (deterioration e.g. time to failure) and outputs. Instead, the latter can be achieved using a surrogate model (the statistical emulator) that would interpolate between the DGM simulation results used as training runs.

Here, the surrogate model is a Gaussian process (GP) which approximates the DGM as a relationship between the training data inputs and outputs. GPs are random (stochastic) processes that are very flexible and can be modeled to mimic the behavior of simple and complicated data, processes, and functions. They can be understood as a limit of multivariate normal distributions as the variability in the process of interest becomes infinite, i.e. a function with continuous output.

GPs are widely used in machine learning for regression and classification problems [78]. In statistical literature, GPs have frequently been used to emulate complex relationships between inputs and outputs for computationally expensive computer experiments due to their flexibility and convenient analytical properties [79,80]. The term "emulator" has originally been applied to GP surrogates, similar to GP regression, that can capture the full range of uncertainty in the underlying model and training data [79], as opposed to deterministic surrogate models. As shown in the next section, GPs can be defined using a set of parameters (emulator parameters) that control its mean and variance functions.

In "black-box" applications of GP emulation, the emulator mean and variance functions are chosen from a predefined, often limited, selection of options, and the parameters can be estimated using numerical optimization. This is the approach typically performed in machine learning and artificial intelligence applications when high volumes of data are available. However, in this work, a custom implementation of a GP emulator was created based on a moderate number of DGM runs and reliable expert engineering knowledge using Bayesian inference and Markov chain Monte Carlo. For examples of the use of GPs in slope stability see Hu et al. [81] and Kang et al. [82,83]. For examples in other geotechnical applications see Pal and Deswal [84] and Yoshida et al. [85].

6.1 Development and evaluation of the Gaussian process emulator

GPs are a highly flexible class of models that can be used to emulate the behaviour of continuous functions, e.g., the DGM simulations. This section is used to introduce the development of the Gaussian process emulator (GPE). The emulator outlined here can predict some scalar output y for an input x that can be a collection of parameters (geometry, soil properties, etc.). This can be extended to applications where y is a vector using the theory of multivariate normal distributions. For more detail see Svalova et al. [64], where the utility of these methods in this context is established.

Assume that the geotechnical model can be represented by a relationship $f(x) = y$, x and y are inputs and outputs, respectively, and f is the true deterministic numerical computer model. A GP emulator (GPE) is then some function $\eta \approx f$ which emulates the relationship between x and y. A GP η is a stochastic process fully defined by mean and variance functions $m(\cdot)$ and $\Sigma(\cdot, \cdot)$, $\eta \sim GP(m(\cdot),\Sigma(\cdot, \cdot))$. The two functions take x as input, where x can be p-dimensional. When η is evaluated at a finite collection of N inputs, $\boldsymbol{x} \in \mathbb{R}^n \times \mathbb{R}^p$, it produces outputs in the form of a distribution of y with the most likely value and uncertainty ranges. Here, $p = 5$ and the inputs are slope height (x_1), slope angle cotangent (x_2), peak effective cohesion (x_3), peak friction angle (x_4), and near surface reference hydraulic conductivity (x_5). The outputs y can either be any model output value or time series. In this case, y is the time to ultimate limit state failure.

In black-box applications of GPs, $m(x)$ is often set to be zero, however it can be selected to broadly reflect the mean behavior of y as x changes. In this work, it was set to be a linear combination of the inputs, i.e. $m(x) = h(x)^T\boldsymbol{\beta}$ where $h(x) = (1,x_1,x_2,\ldots,x_p)$ and $\boldsymbol{\beta} = (\beta_0,\beta_1,\ldots,\beta_p)^T$ as such the emulator mean function is similar to a regression.

The covariance function between any two inputs x and x'often has a form $\Sigma(x,x',\boldsymbol{\theta}) = \sigma^2 \left(C(x,x',\boldsymbol{\theta}) + \tau\mathbb{I}(x,x')\right)$, where σ^2 is the scale parameter, C is a correlation function which has a maximum when $x = x'$ and decays to zero as the distance between x and x' increases. In other words, C ensures that

outputs that have similar inputs will be more strongly correlated than otherwise. τ is a "nugget" parameter added for numerical stability [86], and $\mathbb{I}$ is an indicator function which is one when $x = x'$ and zero otherwise. $\boldsymbol{\theta} = (\theta_1,\theta_2,...,\theta_p)^T$ is the vector of correlation lengths (lengthscales), whereby large values lead to "smoother" behaviors. Here, a twice-differentiable Matern correlation function was adopted [78].

One of the advantages of using GPs as surrogate models is that it is possible to condition η on observations y using analytical properties of multivariate normal distributions, which makes computation straightforward. Assume that $\boldsymbol{y} = (\eta(x_1),...,\eta(x_N))^T$ is a training set of numerical model outputs evaluated at inputs $\boldsymbol{x}_1,\boldsymbol{x}_2,...$ $\boldsymbol{x}_N$, $\boldsymbol{x}_i = (x_1,...x_p)^T$. The distribution of η conditional on the training data is also a GP, $\eta^*(\cdot) \sim GP(m^*(\cdot),\Sigma^*(\cdot,\cdot))$, where $m^*(x) = h^T(x)\boldsymbol{\beta} + t(x)^T\Sigma_x^{-1}(y - H_x\beta)$ and $\Sigma^*(x,x') = \sigma^2(C(x,x',\boldsymbol{\theta}) - t(x)^T\Sigma_x^{-1}t(x'))$. In these functions, the $N \times N$ matrix Σ_x is the covariance function evaluated on the training data, H_x is the $N \times (p+1)$ regressor matrix whose i-th row is $h(x_i)$. This formalism is possible when it is assumed that $\boldsymbol{y}$ follows a normal distribution with mean $H_x\boldsymbol{\beta}$ and variance Σ_x, $\boldsymbol{y} \sim N(H_x\boldsymbol{\beta},\Sigma_x)$. Also, $t(z) = (C(z,\boldsymbol{x}_1,\boldsymbol{\theta}),C(z,\boldsymbol{x}_2,\boldsymbol{\theta}),...,C(z,\boldsymbol{x}_N,\boldsymbol{\theta}))^T$ is a vector of correlations between some inputs z and the training data $\boldsymbol{x}_1,\boldsymbol{x}_2,...,\boldsymbol{x}_N$. This conditional relationship of a GP on the normally-distributed training data is the analytical apparatus which allows interpolation between the training data points. Note that it is not advised to use η^* for inputs that are far outside the range of the training data inputs as the uncertainty will be very high.

6.2 Bayesian inference and Markov chain Monte Carlo simulation

The choice of parameters controlling η is non-trivial, and numerical optimization can fail to produce good estimates for models of high complexity and sparse training data. Additionally, such parameter estimates can often come without uncertainty ranges or have extreme values far exceeding the range of the real value. Bayesian inference can help to mitigate these issues, as inference on model parameters can be informed using the training data as well as expert judgement.

Assume that $\Theta = (\boldsymbol{\beta},\sigma^2,\boldsymbol{\theta},\tau)$ is the vector of emulator parameters. Information about the data $\boldsymbol{y}$ is summarized by the likelihood function $L(\Theta;\boldsymbol{y})$, which here is the probability density function of $\boldsymbol{y}$, $N(H_x\boldsymbol{\beta},\Sigma_x)$. Expert judgement is also formalized using a probability distribution, known as the prior distribution $\pi(\Theta)$, using engineering opinion. For example, in modeling slope time to failure (TTF) as a function of the slope properties, the mean function $m(x)$ is, in effect, a regression, where β_0 can be understood as "baseline" time to failure when the remaining inputs are zero. As slopes with zero apparent cohesion and a friction angle less than the slope angle would be inherently unstable and so expected to fail immediately, β_0 would have some probability distribution centered around zero and having a narrow spread, such as a normal distribution with a mean of zero and variance of one. The distributions for β_1 can be elicited by considering that it is expected that TTF will decrease with an increase in height, which would imply a negative mean value for β_1. The remaining β_2- β_5 can be obtained in a similar manner. If eliciting engineering opinion for $\boldsymbol{\beta}$ is difficult, their mean values can be set at zero and reasonable orders of magnitude can be estimated by performing linear regression on $\boldsymbol{y}$ against $\boldsymbol{x}$.

Using Bayes' theorem, we can obtain the "posterior" distribution of Θ using data and expert opinion, $\pi(\Theta|\boldsymbol{y})$ where the expression inside the brackets means "Θ given $\boldsymbol{y}$", which is proportional to the product of the prior

distribution and the likelihood, $\pi(\Theta|\boldsymbol{y}) \propto \pi(\Theta) \times L(\Theta;\boldsymbol{y})$. Often, $\pi(\Theta|\boldsymbol{y})$ is very difficult to obtain analytically, therefore we use Markov chain Monte Carlo (MCMC) sampling to estimate it. A custom MCMC estimation procedure was implemented in R Statistical Software [87]. The interested reader can see more details in Svalova et al. [64] and the supplementary material therein.

7 Exemplar forecasting outputs

The emulator described in Section 6 can produce output in a number of forms. These include projections of time to failure for a range of geometries with specified values of the input parameters. It can also produce the empirical cumulative distribution function (ECDF) of the percentage of failed slopes with time for a specified grouping of slope properties and geometries, which introduces a probabilistic element into the results. Examples of these are provided in this section.

7.1 Emulated time to failure

Plots of time to failure for differing slope geometries are summarized in Figure 12. The figure subplots (a, b, c and d), adopt specific values of the shear strength properties and reference hydraulic conductivity representing the range of published values for London Clay in addition to values used in prior modeling work.

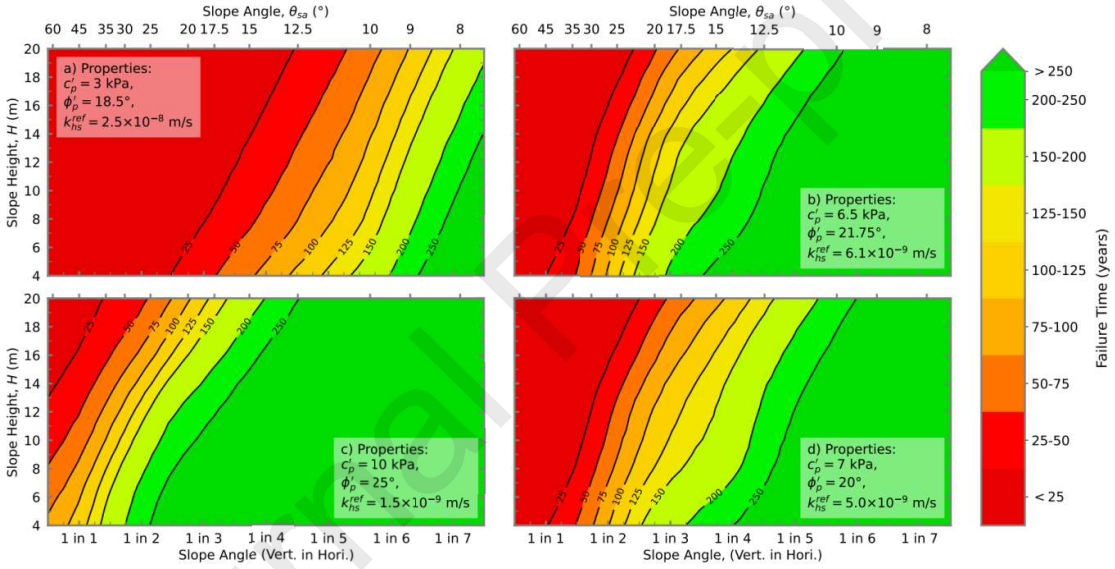

Figure 12: Emulator output showing time to failure for varying cut slope geometries for specified strength and hydraulic conductivity; a) the minimum strength and maximum hyd. conductivity; b) the median of the properties; c) the maximum strength and minimum hydraulic conductivity, d) properties representative of London Clay as used in previous cut slope modeling studies [e.g. 36,38].

From examination of Figure 12, it is clear that time to failure decreases with increasing slope height and increasing slope angle. For both highways cuttings on the M4 motorway and railway cut slopes on the GWML, the majority of the slopes sit in the range of 2 to 8 m in height and angles of 1 in 1.5 to 1 in 3.5 (see Figure 8). For the commonly adopted peak strength and hydraulic conductivity properties for London Clay (Figure 12d), and for the 8 m high slopes in the 1 in 1.5 to 1 in 3.5 grouping, this gives a range of potential time to failure from 25 to 200 years.

It is also clear that the time to failure of a given slope geometry increases with increasing shear strength and decreasing hydraulic conductivity. The specific effect of each of these properties on failure is explored in more detail in the emulated ECDF results.

7.2 Emulated probability of failure

The primary difference between the plots of time to failure in Figure 12 and the ECDF plots is that the former provide a discrete estimate of time to failure for a specific set of properties, whereas the latter allow the probability of failure for a range of properties or model geometries to be derived. Note that the comparisons are made at a probability of failure of 50% ($P_f = 0.5$) as the FoS of a slope at $P_f = 0.5$ is generally regarded to be 1; see the discussion in Silva et al. [88]. Also note that the interpretation of $P_f = 0.5$ for a group of differing slopes as per the $1 - \text{ECDF}$ of time to failure is the proportion of that group which have failed. In this case, the use of $P_f = 0.5$ is primarily intended to aid consistent comparison between distinct deterioration curves and is not intended as an appropriate design value.

To facilitate network-scale deterioration analyses of long-linear assets (in this case slopes), the proportion of stable slopes within a network at a given age can be derived as $1 - \text{ECDF}$ of the time to failure at that age. Plots of the declining proportion of stable slopes with time (presented in percentage) for the full range of HP-OC cut slopes on the GWML and M4 between London and Bristol, and the full range of potential material properties adopted in this study can be seen for varying heights in Figure 13 and for varying slope angles in Figure 14.

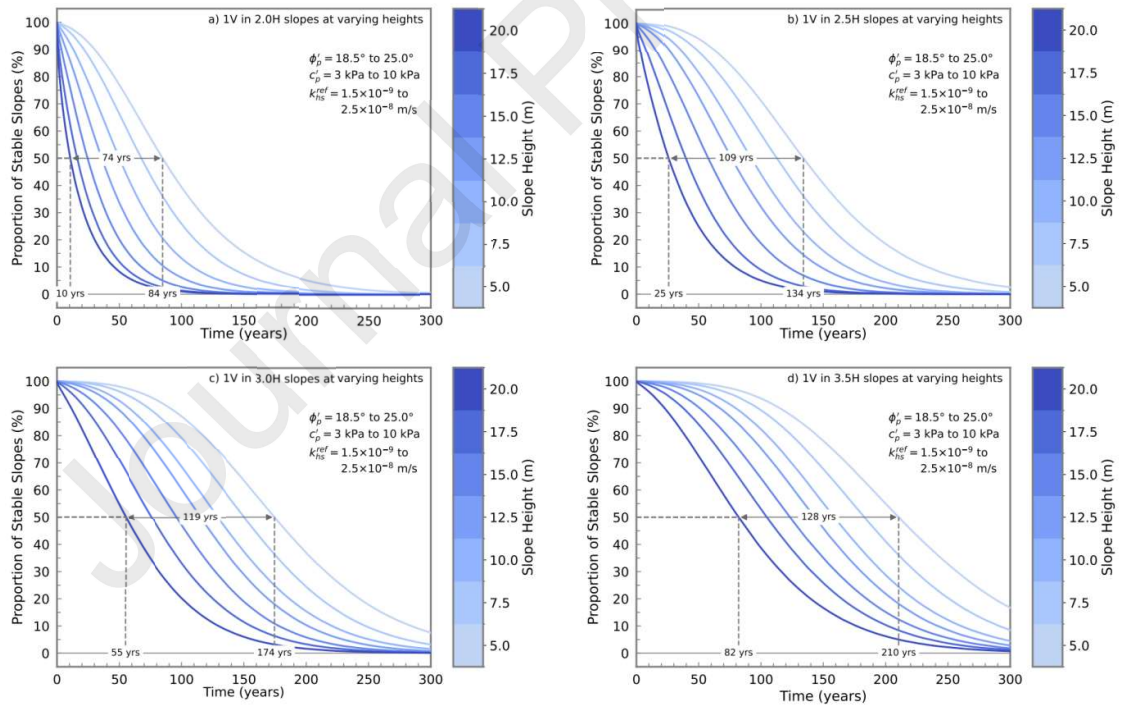

Figure 13: Proportion of stable slopes of varying heights at angles of a) 1V in 2.0H; b) 1V in 2.5H; c) 1V in 3.0H; d) 1V in 3.5H as a function of time from end of construction. NB the times to failure for $P_f = 0.5$ are intended to aid comparison only and are not recommended design values.

The proportion of stable slopes, as shown in Figure 13 and Figure 14, increases with decreasing slope height and/or slope angle. The figures also demonstrate that the effects of varying slope height and slope angle on

stability are not independent as the range of time to failure when varying height from 5 to 20 m increases, as the slope angle decreases. This is illustrated in Figure 13a and Figure 13d, where there is a difference in predicted time to failure of 74 years between a height of 5 m and 20 m, for the 1 in 2 slopes for $P_f =$ 0.5. The difference increases to 128 years for slopes at 1 in 3.5.

Figure 15 illustrates the effect of varying the material properties on the proportion of stable slopes, showing a similar pattern to that seen in Figure 12, whereby, for a given shear strength parameter, c'_p or ϕ'_p, (Figure 15a and b), the proportion of stable slopes at a given time increases with increasing shear strength. The differences in specific times to failure presented for $P_f =$ 0.5, indicate the relative effect of the individual parameters and their assumed ranges on the modeled time to failure.

Where near surface reference hydraulic conductivity is varied (Figure 15c), the proportion of stable slopes at a given time increases with decreasing near-surface hydraulic conductivity. Figure 15d shows the change in rates of failure with time for the full range of modeled parameters. The overall range of time to failure is 228 years with a minimum value of 25 years assuming the worst-case soil properties and 253 years assuming the best case (the adopted material properties can be seen in Table 3). The general implications of the results are discussed in Section 8.

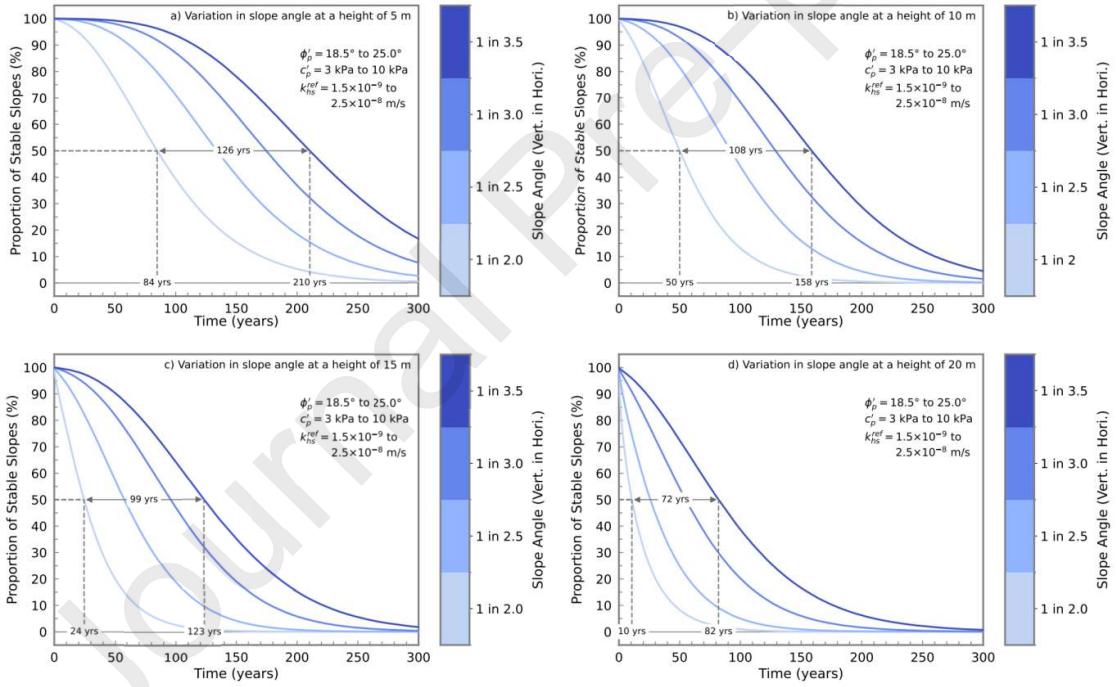

Figure 14: Proportion of stable slopes of varying slope angles at heights of a) 5 m; b) 10 m; c) 15 m; d) 20 m as a function of time from end of construction. NB the times to failure for a probability of 0.5 are intended to aid comparison only and are not recommended design values.

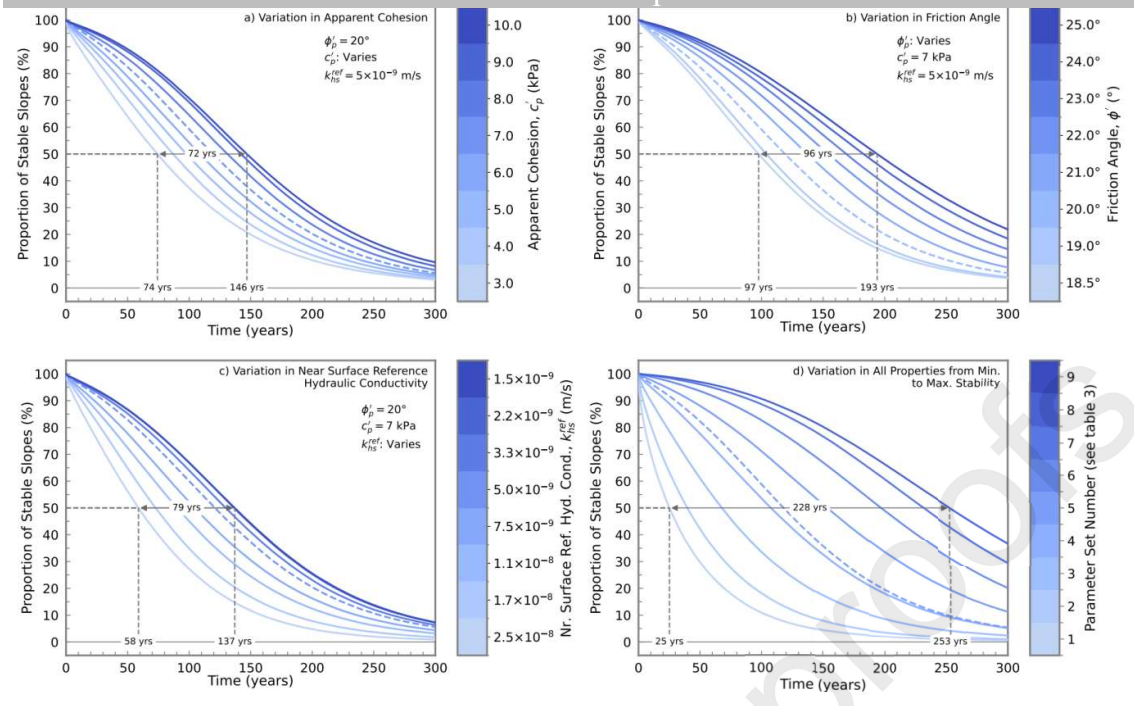

Figure 15: Proportion of stable slopes with time for variations in the assumed properties; a) varying apparent cohesion; b) varying friction angle; c) varying reference hydraulic conductivity; d) variation in all material properties as per Table 3 and applied to the full range of slope geometries. The dashed curve represents the behaviour for typical London Clay properties. *NB the times to failure for a probability of 0.5 are intended to aid comparison only and are not recommended design values.*

Table 3: Properties of the emulated parameter sets in Figure 15d, adopted to show the range of potential modeled behaviour.

Parameter Set No.	Cohesion, c'_p (kPa)	Friction, ϕ'_p(°)	Ref. Hyd. Conductivity, k_{hs}^{ref} (m/s)
1	3.0	18.5	2.50×10^{-8}
2	4.0	19.0	1.67×10^{-8}
3	5.0	20.0	1.12×10^{-8}
4	6.0	21.0	7.49×10^{-9}
5	7.0	20.0	5.00×10^{-9}
6	7.0	22.0	5.00×10^{-9}
7	8.0	23.0	3.35×10^{-9}
8	9.0	24.0	2.24×10^{-9}
9	10.0	25.0	1.50×10^{-9}

8 Discussion and implications

The results summarized in Section 7 indicate the significant effects of slope geometry and soil mechanical and hydraulic properties on the potential time to failure of slopes. In this section, these results are set into the context of the age of existing UK rail and highways transport infrastructure slopes and the proposed design life of future UK High Speed 2 (HS2) railway slopes. The intended use of these results is also discussed along with the effects that a number of the key assumptions about the modeling may have on their interpretation.

8.1 Slope angle and height

The emulated model results demonstrate the effect of slope geometry on the time to failure of cut slopes in overconsolidated high plasticity clays. Figure 12 demonstrates the relatively high sensitivity of the time to failure to varying slope angle. For example, reducing slope angle from 1V in 2H to 1V in 3H for a 10 m high cut slope results in an increase in the time to failure from 50-75 years to 125-150 years (see Figure 12b). This indicates the benefit of adopting less steep slope angles at the design phase, in situations where there are specific design life requirements. That is, a 1V in 2H slope may meet 60-year design life criteria for road and rail, but would need to be decreased to a 1V in 3H slope to meet a requirement for a 120-year serviceable life [for UK highways slopes see Ref. 12] or HS2 120-year design life [89].

Figure 13 illustrates the large effect slope height has on time to failure, where for a common slope angle (1 in 3), and for $P_f = 0.5$ (*i.e.*, FoS = 1.0), a decrease in slope height from 20 m to 5 m leads to an increase in service life from 55 to 174 years. This is primarily of interest when evaluating the potential deterioration of existing earthworks. However, it may also be a consideration when selecting route alignment in new transport corridor designs. In summary, Figure 13 and Figure 14 show the ability of the emulator to assist in probabilistic design assessments of slope geometry, whereby for specified design life and probability of failure, minimum cut slope angles could be defined.

In order to better visualize the effect of slope geometry on time to failure, and how this compares with assumed design life, the data used to produce Figure 12 was replotted as slope angle versus time to failure for varying slope heights, as shown in Figure 16. The material properties selected are representative of the worst and best cases in terms of effect on time to failure, along with the mean of the range of properties for the London Clay.

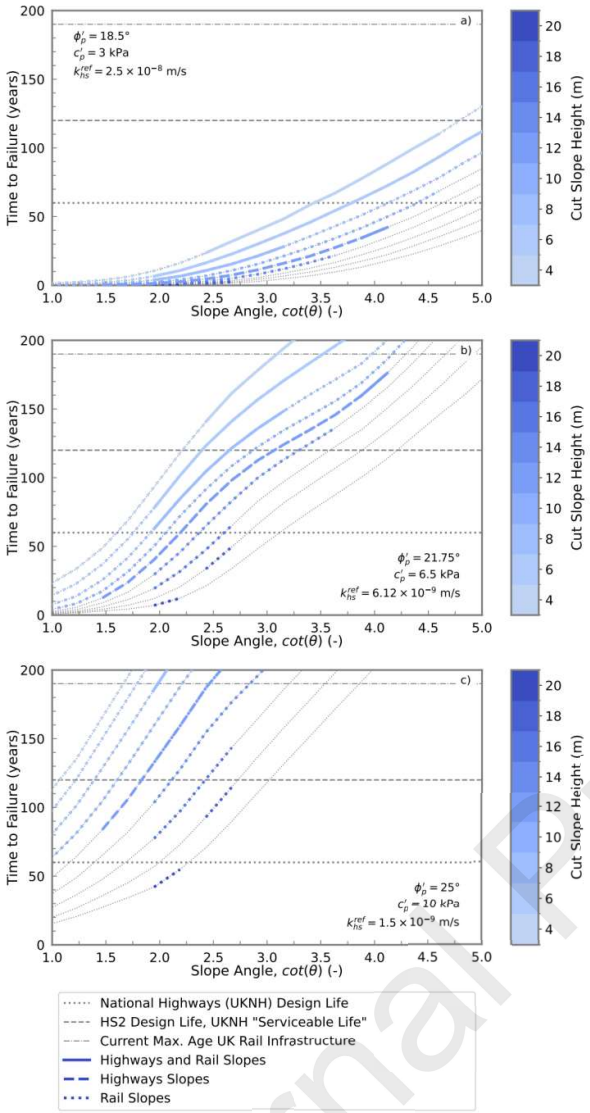

Figure 16: The time to failure for differing slope geometries and asset types (highways vs rail) considering the range of adopted material properties of the London Clay, annotated with typical design life values and the current maximum age of UK railways slope infrastructure, a) lowest stability properties; b) mean properties; c) maximum stability properties.

This plot demonstrates how the emulator could produce stability charts that bring the temporal element into the stability assessment, alongside strength properties and slope geometry that are more commonly found in this type of chart. This is similar to the approach used in Postill et al. [62]. The plot also separates out the typical range of slope heights formed within OC-HP clays seen on the GWML railway from those seen on the M4 motorway.

Figure 16a shows the time to failure data for the worst-case scenario. This suggests that while the adopted parameters may have plausible values to represent a discrete soil element based on laboratory testing, they may not be appropriate for the soil mass as a whole based on indicated times to failure.

The properties that represent the mean of the dataset produce more plausible results for the highways slopes with heights up to 12 m, giving times to failure larger than 60 years for slope angles less than 1V in 2.5H and times to failure greater than 120 years for slope angles less than 1V in 3.0H for the slopes analyzed as seen in Figure 16b. Ultimately the parameters adopted appear to be rather conservative for the mass properties of the OC-HP clays slopes encountered on the GWML and the M4. This may in part be related to the lack of discrimination between types of failure, with some models undergoing superficial shallow failures that would not be significant so affecting the emulator results.

The Mair review into the Carmont / Stonehaven train derailment in the UK [20] published guidance stating that for high plasticity clays of the type discussed in this work, slope angles should be kept below 14 degrees (≈ 1V in 4H) to maintain stability.

The modeling undertaken herein suggests that this proposed maximum slope angle may be appropriate for the assumed mean strength and permeability properties used in the modeling for both road and rail cut slopes (assumed to have been excavated in the 1960s and 1830s respectively) with heights up to 20 m (the limit of the modeled range) for the road slopes to meet a 120-year serviceable life and heights up to approximately 10 m for rail slopes to maintain stability to the present day (i.e. 185 year life, see Figure 16b).

For slopes modeled using the high stability properties, a slope angle of 1V in 4H would be appropriate for all slope heights, for both road and rail (see Figure 16c). This is not the case however, for the modeled slopes with the worst-case properties (see Figure 16a), where failures tend to occur at times significantly less than the age of the GWML rail slopes, and less than the 120-year serviceable life required for UK highways slopes. This is indicative that the low stability property estimate is likely overly conservative for mass scale, as per the prior discussion, but may give a useful lower bound to stable asset life.

Additionally, the other OC-HP materials on the routes in question tend to have higher strength values than the London Clay based on published data [see, for example, the peak strength values for Kimmeridge, Ampthill and Oxford Clay in Figure 9 as per Ref. 69], so the results presented here are inherently conservative. Furthermore, there are a number of additional factors that will act to affect the results as discussed in Section 8.2.

The effect of the adopted shear strength and hydraulic conductivity parameters on the time to failure is shown in Figure 16. The figure provides an indication of the sensitivity of the time to failure to the adopted properties for a single soil type and the resultant uncertainty this represents for design life. It is clear that adopting the worst-case values would likely require very conservative design slope geometries or a very low threshold for further assessment or monitoring of an existing section of an asset portfolio (assuming this was the approach adopted for assets deemed to have undergone significant deterioration). Conversely, adoption of the best-case properties would likely miss potential failures and significantly overestimate stability (although not an issue in this case as the soil selected for parameter derivation had properties that were conservative). As such, deriving a characteristic value of the parameters for a given asset of interest, that are representative of the zone of ground controlling the behavior [as per Eurocode 7; 90], as opposed to a point minimum, seems appropriate in this case. The previous discussion, along with the probabilistic underpinnings in Eurocode 7, suggest this would potentially be a sensible methodology to adopt in using the emulator approach in a practical setting.

8.2 Additional factors affecting model results

The geotechnical analyses performed as input for the emulator are for an idealized problem, with local weather [Newbury in the South of the UK, see 36] and where climate change [known to be a significant issue, see 38] has been omitted. Furthermore, a uniform material with a simple stress history was simulated, whereas, in reality, engineered slopes have very complex stress histories and spatial variability of material properties exists, where for example, the rate of softening to residual will affect time to failure [62], however a single softening rate is adopted in this study. For cut slopes, the presence of structural discontinuities can also control slope behavior. Surface-vegetation-atmosphere interaction behavior is known to be significant in slope stability [91], but in this work, the effect of vegetation rooting on near surface shear strength has been omitted [see for example 92] and only grass slopes are analyzed, but vegetation type is significant in seasonal pore water pressure cycles [3].

In transportation infrastructure, the deterioration in stiffness and strength due to cyclic vehicle loading, can be significant but is not addressed in this work. The behavior is illustrated in [93] and discussed in the context of slope stability in [50]. It is also recognized that two-dimensional analyses produce conservative factor of safety estimates when compared to three-dimensional analyses [94,95]. The emulated model results illustrated here also do not discriminate between different types of failure (shallow / superficial translational slides versus deep seated rotational mechanisms, for example). As such, the plots of proportion of stable slopes may exaggerate the rate of deterioration as they indicate any failure, no matter the severity and proportion of the slope affected. The failure type can be accounted for in the emulator if this methodology were adopted in practice.

This study presented a framework for rapidly evaluating the time to failure of geotechnical assets that informs design life and estimates of current deterioration, however the following factors should be carefully considered:

- Geotechnical materials are spatially and temporally heterogenous which can have a significant effect on slope behavior [1,30,96–98,99].
- Site-specific issues such as the presence and orientation of pre-existing discontinuities or other stratigraphic features, localized drainage failure, and land use changes can all affect stability and by the nature of this work will not be accounted for.
- Vegetation and vegetation management [3,39,100] can have a significant impact on stability; however, only an unchanging grass cover was included in this work.
- Weather and climate are variable [101,102] and this can affect time to failure of slopes [36,38,103,104]

The above should make it clear that general guidance is inappropriate for specific cases. In particular, high-risk projects in complex ground conditions require detailed analysis of material behavior and other influencing factors.

9 Conclusions

A validated, physically based, deterministic modeling capability has been developed that can simulate the hydro-mechanically coupled behavior of cut and embankment slopes and their deterioration as driven by weather and climate. Model validation was performed against laboratory data and long-term field

monitoring data, emphasizing the importance of high-quality long duration monitoring data and trial field sites.

In parallel, a statistical (Gaussian process) emulator model has also been developed to allow the rapid emulation of physically based modeling results. The emulator was then trained with data from a deterministic modeling parametric study using a formal experimental design approach, making use of Latin hypercube sampling. The modeling framework was used for the characterization of deterioration in overconsolidated clay cut slopes for a range of slope geometries, representative of UK road and rail infrastructure.

The statistical (Gaussian process) emulator allows rapid assessments of likely time to failure to be made for varying slope geometries and with varying material properties. This can be utilized during slope stability analysis to evaluate design life and also in the assessment of existing earthworks both individually and as asset groups (e.g., a transport corridor or network). This allows estimates to be made of the likely degree of deterioration and potential remaining serviceable life. This was demonstrated in this work for cut slope geometries derived from design and survey data for a section of the UK highways network (the M4 between London and Bristol) and from LiDAR surveys of the Great Western Main Line railway (between London and Bristol). In principle this modeling approach could be applied to any asset type for which physically based numerical models can be developed and is of particular utility where these models are computationally intensive and therefore time consuming to run. The broad applicability of this approach to infrastructure deterioration assessment potentially makes it a powerful tool to address some of the key issues highlighted by the UK National Infrastructure Commission.

Acknowledgements

The work presented is an output of the collaborative programme grant ACHILLES (programme grant number EP/R034575/1) funded by the UK Engineering and Physical Sciences Research Council (EPSRC). The field instrumentation data from the highways cut slope used in the validation of the cutting numerical model was provided by Dr. J. Smethurst and Dr. A. Blake of Southampton University and was funded by the UK EPSRC via grant numbers GR/R72341/01 and EP/F063482/1. The data from the BIONICS embankment used in the embankment modeling validation was provided by Dr. P. Hughes (Durham University) and Dr. R. Stirling (Newcastle University) and was produced as part of the UK EPSRC BIONICS (GR/S87430/01) and iSMART (EP/K027050/1) grants. Dr. A. Smith acknowledges the support of a Philip Leverhulme Prize in Engineering (PLP-2019-017). The slope geometry data for the M4 motorway along with processed LiDAR data for the Great Western Main Line railway used to produce Figure 8 were provided by National Highways and Network Rail and collated by Dr. C. Power of Mott MacDonald.

The funding body played no part in the study design; nor in the collection, analysis or interpretation of the data used in this publication; or in its preparation.

The data used in the preparation of the figures in this publication is available from an institutional data repository with the following doi: 10.25405/data.ncl.22714831. The emulator code and the data used as emulator input is available via the following doi numbers: 10.25405/data.ncl.14447670.v2; 10.25405/data.ncl.14331314.v2

Funding

This work was supported by the UK Engineering and Physical Sciences Research Council (EPSRC) [grant numbers EP/R034575/1, GR/R72341/01, EP/F063482/1, GR/S87430/01, EP/K027050/1]; Dr. A. Smith acknowledges the support of a Philip Leverhulme Prize in Engineering [grant number PLP-2019-017].

References

[1] Stirling RA, Toll DG, Glendinning S, Helm PR, Yildiz A, Hughes PN, et al. Weather-driven deterioration processes affecting the performance of embankment slopes. Géotechnique 2021;71:957–69. https://doi.org/10.1680/jgeot.19.SiP.038.

[2] Kodikara J, Islam T, Sounthararajah A. Review of soil compaction: History and recent developments. Transp Geotech 2018;17:24–34. https://doi.org/10.1016/j.trgeo.2018.09.006.

[3] Briggs KM, Smethurst JA, Powrie W, O'Brien AS. The influence of tree root water uptake on the long term hydrology of a clay fill railway embankment. Transp Geotech 2016;9:31–48. https://doi.org/10.1016/j.trgeo.2016.06.001.

[4] Clarke D, Smethurst JA. Effects of climate change on cycles of wetting and drying in engineered clay slopes in England. Q J Eng Geol Hydrogeol 2010;43:473–86. https://doi.org/10.1144/1470-9236/08-106.

[5] Lowe JA, Bernie D, Bett P, Bricheno L, Brown S, Calvert D, et al. UKCP18 science overview report. Exeter: Met Office Hadley Centre; 2018.

[6] Füssel H-M, Kristensen P, Jol André, Marx A, Hildén M. Climate change, impacts and vulnerability in Europe 2016: an indicator-based report. Luxembourg: Publications Office of the European Union; 2017.

[7] IPCC. Climate Change 2021: The Physical Science Basis. Contribution of Working Group I to the Sixth Assessment Report of the Intergovernmental Panel on Climate Change. Cambridge, UK and New York, NY, USA: Intergovernmental Panel on Climate Change; 2021. https://doi.org/10.1017/9781009157896.

[8] Vardon PJ. Climatic influence on geotechnical infrastructure: a review. Environ Geotech 2015;2:166–74. https://doi.org/10.1680/envgeo.13.00055.

[9] Jacobs JM, Culp M, Cattaneo L, Chinowsky PS, Choate A, DesRoches S, et al. Chapter 12 : Transportation. Impacts, Risks, and Adaptation in the United States: The Fourth National Climate Assessment, Volume II. U.S. Global Change Research Program; 2018. https://doi.org/10.7930/NCA4.2018.CH12.

[10] National Research Council of the National Academies. Potential impacts of climate change on U.S. transportation. Washington, D.C.: Transportation Research Board; 2008.

[11] Network Rail. Earthworks Technical Strategy. Milton Keynes: Network Rail; 2018.

[12] Daly T, Carluccio S, Bhanderi D, Patterson D, Power C, Codd J. Use of Geotechnical Asset Data Within Highways England: The Journey so Far and the Future. In: Correia AG, Tinoco J, Cortez P, Lamas L, editors. Inf. Technol. Geo-Eng., Cham: Springer International Publishing; 2020, p. 797–812. https://doi.org/10.1007/978-3-030-32029-4_68.

[13] Skempton AW. Embankments and cuttings on the early railways. Constr Hist 1995;11:33–49.

[14] Briggs KM, Loveridge FA, Glendinning S. Failures in transport infrastructure embankments. Eng Geol 2017;219:107–17. https://doi.org/10.1016/j.enggeo.2016.07.016.

[15] O'Brien AS. Rehabilitation of urban railway embankments: investigation, analysis and stabilisation. In: Cuéllar V, Dapena E, Alonso E, Echave JM, Gens A, De Justo JL, et al., editors. Proc. 14th Eur. Conf. Soil Mech. Geotech. Eng., Madrid: Millpress, Amsterdam, the Netherlands; 2007, p. 125–43.

[16] Perry J, Pedley M, Reid M. Infrastructure Embankments – Condition Appraisal and Remedial Treatment (C592). London: Construction Industry Research and Information Association.; 2003.

[17] Charlesworth G. A History of British Motorways. London, UK: Thomas Telford Ltd; 1984. https://doi.org/10.1680/ahobm.01596.

[18] Perry J, Pedley M, Brady K. Infrastructure Cuttings - Condition Appraisal and Remedial Treatment (C591). London: Construction Industry Research and Information Association.; 2003.

[19] Highways England. Design Manual for Roads and Bridges: Managing the maintenance of highway geotechnical assets 2020.

[20] Mair R. A Review of Earthworks Management. Milton Keynes: Network Rail; 2021.

[21] National Infrastructure Commission. The Second National Infrastructure Assessment: Baseline Report. National Infrastructure Commission; 2021.

[22] Conti S, Gosling JP, Oakley JE, O'Hagan A. Gaussian process emulation of dynamic computer codes. Biometrika 2009;96:663–76. https://doi.org/10.1093/biomet/asp028.

[23] Gramacy RB. Surrogates: Gaussian Process Modeling, Design, and Optimization for the Applied Sciences. Chapman and Hall/CRC; 2020. https://doi.org/10.1201/9780367815493.

[24] Santner TJ, Williams BJ, Notz WI. The Design and Analysis of Computer Experiments. New York, NY: Springer New York; 2018. https://doi.org/10.1007/978-1-4939-8847-1.

[25] Xu Z, Wang X. Global sensitivity analysis of the reliability of the slope stability based on the moment-independent combine with the Latin hypercube sampling technique. Stoch Environ Res Risk Assess 2023. https://doi.org/10.1007/s00477-023-02385-5.

[26] Baudin M. pyDOE: The Experimental Design Package for Python - Randomized Designs 2013. https://pythonhosted.org/pyDOE/randomized.html (accessed November 18, 2019).

[27] Itasca. Fast Lagrangian Analysis of Continua v. 8.0 - User's Guide. Minneapolis: Itasca Consulting Group Inc.; 2016.

[28] Dixon N, Bromhead EN. Depth-dependent permeability in London Clay measured using standpipe piezometer equilibration data. Géotechnique 1999;49:651–60. https://doi.org/10.1680/geot.1999.49.5.651.

[29] Hight DW, Gasparre A, Nishimura S, Minh NA, Jardine RJ, Coop MR. Characteristics of the London Clay from the Terminal 5 site at Heathrow Airport. Géotechnique 2007;57:3–18. https://doi.org/10.1680/geot.2007.57.1.3.

[30] Dixon N, Crosby CJ, Stirling R, Hughes PN, Smethurst J, Briggs K, et al. In situ measurements of near-surface hydraulic conductivity in engineered clay slopes. Q J Eng Geol Hydrogeol 2019;52:123–35. https://doi.org/10.1144/qjegh2017-059.

[31] Samarasinghe AM, Huang YH, Drnevich VP. Permeability and Consolidation of Normally Consolidated Soils. J Geotech Eng Div 1982;108:835–50. https://doi.org/10.1061/AJGEB6.0001305.

[32] van Genuchten MTh. A Closed-form Equation for Predicting the Hydraulic Conductivity of Unsaturated Soils. Soil Sci Soc Am J 1980;44:892–8. https://doi.org/10.2136/sssaj1980.03615995004400050002x.

[33] Croney D. The Design and Performance of Road Pavements. London: Her Majesty's Stationery Office; 1977.

[34] Morsy AM, Helm PR, El-Hamalawi A, Smith A, Hughes PN, Stirling RA, et al. Development of a Multiphase Numerical Modeling Approach for Hydromechanical Behavior of Clay Embankments Subject to Weather-Driven Deterioration. J Geotech Geoenvironmental Eng 2023;149:04023062. https://doi.org/10.1061/JGGEFK.GTENG-11213.

[35] Ellis EA, O'Brien AS. Effect of height on delayed collapse of cuttings in stiff clay. Proc Inst Civ Eng - Geotech Eng 2007;160:73–84. https://doi.org/10.1680/geng.2007.160.2.73.

[36] Postill H, Helm PR, Dixon N, Glendinning S, Smethurst JA, Rouainia M, et al. Forecasting the long-term deterioration of a cut slope in high-plasticity clay using a numerical model. Eng Geol 2021;280:105912. https://doi.org/10.1016/j.enggeo.2020.105912.

[37] Potts DM, Kovacevic N, Vaughan PR. Delayed collapse of cut slopes in stiff clay. Géotechnique 1997;47:953–82. https://doi.org/10.1680/geot.1997.47.5.953.

[38] Rouainia M, Helm P, Davies O, Glendinning S. Deterioration of an infrastructure cutting subjected to climate change. Acta Geotech 2020;15:2997–3016. https://doi.org/10.1007/s11440-020-00965-1.

[39] Tsiampousi A, Zdravkovic L, Potts DM. Numerical study of the effect of soil–atmosphere interaction on the stability and serviceability of cut slopes in London clay. Can Geotech J 2017;54:405–18. https://doi.org/10.1139/cgj-2016-0319.

[40] Kulhawy FH, Duncan JM, Seed HB. Finite element analyses of stresses and movements in embankments during construction. Vicksburg, Mississippi: U.S. Army Engineers, Waterways Experiment Station, Corps of Engineers; 1969.

[41] Burland JB. On the compressibility and shear strength of natural clays. Géotechnique 1990;40:329–78. https://doi.org/10.1680/geot.1990.40.3.329.

[42] Leroueil S, Vaughan PR. The general and congruent effects of structure in natural soils and weak rocks. Géotechnique 1990;40:467–88. https://doi.org/10.1680/geot.1990.40.3.467.

[43] Skempton AW. First-Time Slides in Over-Consolidated Clays. Géotechnique 1970;20:320–4. https://doi.org/10.1680/geot.1970.20.3.320.

[44] Lupini JF, Skinner AE, Vaughan PR. The drained residual strength of cohesive soils. Géotechnique 1981;31:181–213. https://doi.org/10.1680/geot.1981.31.2.181.

[45] Mesri G, Cepeda-Diaz AF. Residual shear strength of clays and shales. Géotechnique 1986;36:269–74. https://doi.org/10.1680/geot.1986.36.2.269.

[46] Bažant ZP, Pijaudier-Cabot G. Nonlocal Continuum Damage, Localization Instability and Convergence. J Appl Mech 1988;55:287. https://doi.org/10.1115/1.3173674.

[47] Galavi V, Schweiger HF. Nonlocal Multilaminate Model for Strain Softening Analysis. Int J Geomech 2010;10:30–44. https://doi.org/10.1061/(ASCE)1532-3641(2010)10:1(30).

[48] Summersgill FC, Kontoe S, Potts DM. On the use of nonlocal regularisation in slope stability problems. Comput Geotech 2017;82:187–200. https://doi.org/10.1016/j.compgeo.2016.10.016.

[49] Vermeer PA, Brinkgreve RBJ. A new effective non-local strain measure for softening plasticity. In: Chambon R, Desrues J, Vardoulakis I, editors. Int. Workshop Localization Bifurc. Theory Soils Rocks, Rotterdam: 1994, p. 89–100.

[50] Leroueil S. Natural slopes and cuts: movement and failure mechanisms. Géotechnique 2001;51:197–243. https://doi.org/10.1680/geot.2001.51.3.197.

[51] Cooper MR, Bromhead EN, Petley DJ, Grants DI. The Selborne cutting stability experiment. Géotechnique 1998;48:83–101. https://doi.org/10.1680/geot.1998.48.1.83.

[52] Mesri G, Shahien M. Residual Shear Strength Mobilized in First-Time Slope Failures. J Geotech Geoenvironmental Eng 2003;129:12–31. https://doi.org/10.1061/(asce)1090-0241(2003)129:1(12).

[53] Take WA, Bolton MD. Seasonal ratcheting and softening in clay slopes, leading to first-time failure. Géotechnique 2011;61:757–69. https://doi.org/10.1680/geot.9.P.125.

[54] Apted JP. Effects of weathering on some geotechnical properties of London Clay. Imperial College of Science and Technology, University of London, 1977.

[55] Lau WHW. The behaviour of clay in simple shear and triaxial tests. City, University of London, 1988.

[56] Smethurst JA, Clarke D, Powrie W. Seasonal changes in pore water pressure in a grass-covered cut slope in London Clay. Géotechnique 2006;56:523–37. https://doi.org/10.1680/geot.2006.56.8.523.

[57] Smethurst JA, Clarke D, Powrie W. Factors controlling the seasonal variation in soil water content and pore water pressures within a lightly vegetated clay slope. Géotechnique 2012;62:429–46. https://doi.org/10.1680/geot.10.P.097.

[58] Postill H, Dixon N, Fowmes G, El-Hamalawi A, Take WA. Modelling seasonal ratcheting and progressive failure in clay slopes: a validation. Can Geotech J 2020;57:1265–79. https://doi.org/10.1139/cgj-2018-0837.

[59] Glendinning S, Hughes P, Helm P, Chambers J, Mendes J, Gunn D, et al. Construction, management and maintenance of embankments used for road and rail infrastructure: implications of weather induced pore water pressures. Acta Geotech 2014;9:799–816. https://doi.org/10.1007/s11440-014-0324-1.

[60] Hughes PN, Glendinning S, Mendes J, Parkin G, Toll DG, Gallipoli D, et al. Full-scale testing to assess climate effects on embankments. Proc Inst Civ Eng - Eng Sustain 2009;162:67–79. https://doi.org/10.1680/ensu.2009.162.2.67.

[61] Clough RW, Woodward RJ. Analysis of Embankment Stresses and Deformations. J Soil Mech Found Div 1967;93:529–49. https://doi.org/10.1061/JSFEAQ.0001005.

[62] Postill H, Helm PR, Dixon N, El-Hamalawi A, Glendinning S, Take WA. Strength parameter selection framework for evaluating the design life of clay cut slopes. Proc Inst Civ Eng - Geotech Eng 2023;176:254–73. https://doi.org/10.1680/jgeen.21.00125.

[63] Kalantari AR, Johari A, Zandpour M, Kalantari M. Effect of spatial variability of soil properties and geostatistical conditional simulation on reliability characteristics and critical slip surfaces of soil slopes. Transp Geotech 2023;39:100933. https://doi.org/10.1016/j.trgeo.2023.100933.

[64] Svalova A, Helm P, Prangle D, Rouainia M, Glendinning S, Wilkinson DJ. Emulating computer experiments of transport infrastructure slope stability using Gaussian processes and Bayesian inference. Data-Centric Eng 2021;2:e12. https://doi.org/10.1017/dce.2021.14.

[65] Kovacevic N, Hight DW, Potts DM. Predicting the stand-up time of temporary London Clay slopes at Terminal 5, Heathrow Airport. Géotechnique 2007;57:63–74. https://doi.org/10.1680/geot.2007.57.1.63.

[66] Chandler RJ. Lias clay: weathering processes and their effect on shear strength. Géotechnique 1972;22:403–31. https://doi.org/10.1680/geot.1972.22.3.403.

[67] Cripps JC, Taylor RK. The engineering properties of mudrocks. Q J Eng Geol 1981;14:325–46. https://doi.org/10.1144/gsl.qjeg.1981.014.04.10.

[68] Cripps JC, Taylor RK. Engineering characteristics of British over-consolidated clays and mudrocks I. Tertiary deposits. Eng Geol 1986;22:349–76. https://doi.org/10.1016/0013-7952(86)90004-9.

[69] Cripps JC, Taylor RK. Engineering characteristics of British over-consolidated clays and mudrocks, II. Mesozoic deposits. Eng Geol 1987;23:213–53. https://doi.org/10.1016/0013-7952(87)90091-3.

[70] Garga VK. Residual shear strength under large strains and the effect of sample size on the consolidation of fissured clay. University of London (Imperial College of Science and Technology), 1970.

[71] Gourvenec SM, Mair RJ, Bolton MD, Soga K. Ground conditions around an old tunnel in London Clay. Proc Inst Civ Eng - Geotech Eng 2005;158:25–33. https://doi.org/10.1680/geng.2005.158.1.25.

[72] Hight DW, McMillan F, Powell JJM, Jardine RJ, Allenou CP. Some characteristics of London clay. In: Tan TS, Phoon KK, Hight DW, Leroueil S, editors. Proc. Second Int. Workshop Characterisation Eng. Prop. Nat. Soils, vol. 2, Singapore: 2003, p. 851–907.

[73] Sandroni SS. The Strength of London Clay in Total and Effective Stress Terms. Imperial College of Science and Technology, University of London, 1977.

[74] Stark TD, Choi H, McCone S. Drained Shear Strength Parameters for Analysis of Landslides. J Geotech Geoenvironmental Eng 2005;131:575–88. https://doi.org/10.1061/(ASCE)1090-0241(2005)131:5(575).

[75] Bromhead EN, Dixon N. The field residual strength of London Clay and its correlation with laboratory measurements, especially ring shear tests. Géotechnique 1986;36:449–52. https://doi.org/10.1680/geot.1986.36.3.449.

[76] Lupini JF. The *residu*al strength of soils. Imperial College of Science and Technology, University of London, 1980.

[77] Summersgill FC, Kontoe S, Potts DM. Stabilisation of excavated slopes in strain-softening materials with piles. Géotechnique 2018;68:626–39. https://doi.org/10.1680/jgeot.17.P.096.

[78] Rasmussen CE, Williams CKI. Gaussian processes for machine learning. Cambridge, Mass: MIT Press; 2006.

[79] Bastos LS, O'Hagan A. Diagnostics for Gaussian Process Emulators. Technometrics 2009;51:425–38. https://doi.org/10.1198/TECH.2009.08019.

[80] O'Hagan A. Bayesian analysis of computer code outputs: A tutorial. Reliab Eng Syst Saf 2006;91:1290–300. https://doi.org/10.1016/j.ress.2005.11.025.

[81] Hu B, Su G, Jiang J, Xiao Y. Gaussian Process-Based Response Surface Method for Slope Reliability Analysis. Adv Civ Eng 2019;2019:1–11. https://doi.org/10.1155/2019/9185756.

[82] Kang F, Han S, Salgado R, Li J. System probabilistic stability analysis of soil slopes using Gaussian process regression with Latin hypercube sampling. Comput Geotech 2015;63:13–25. https://doi.org/10.1016/j.compgeo.2014.08.010.

[83] Kang F, Xu B, Li J, Zhao S. Slope stability evaluation using Gaussian processes with various covariance functions. Appl Soft Comput 2017;60:387–96. https://doi.org/10.1016/j.asoc.2017.07.011.

[84] Pal M, Deswal S. Modelling pile capacity using Gaussian process regression. Comput Geotech 2010;37:942–7. https://doi.org/10.1016/j.compgeo.2010.07.012.

[85] Yoshida I, Tomizawa Y, Otake Y. Estimation of trend and random components of conditional random field using Gaussian process regression. Comput Geotech 2021;136:104179. https://doi.org/10.1016/j.compgeo.2021.104179.

[86] Neal RM. Monte Carlo Implementation of Gaussian Process Models for Bayesian Regression and Classification. Toronto, Ontario, Canada: University of Toronto; 1997.

[87] R Core Team. R: A language and environment for statistical computing 2021.

[88] Silva F, Lambe TW, Marr WA. Probability and Risk of Slope Failure. J Geotech Geoenvironmental Eng 2008;134:1691–9. https://doi.org/10.1061/(ASCE)1090-0241(2008)134:12(1691).

[89] HS2 Ltd. Transforming lives, building for the future: HS2 Sustainability Approach. Birmingham: High Speed Two (HS2) Limited; 2017.

[90] BSI. BS EN 1997-1:2004+A1:2013: Eurocode 7. Geotechnical design. General rules 2013.

[91] Elia G, Cotecchia F, Pedone G, Vaunat J, Vardon PJ, Pereira C, et al. Numerical modelling of slope–vegetation–atmosphere interaction: an overview. Q J Eng Geol Hydrogeol 2017;50:249–70. https://doi.org/10.1144/qjegh2016-079.

[92] Woodman ND, Smethurst JA, Roose T, Powrie W, Meijer GJ, Knappett JA, et al. Mathematical and computational modelling of vegetated soil incorporating hydraulically-driven finite strain deformation. Comput Geotech 2020;127:103754. https://doi.org/10.1016/j.compgeo.2020.103754.

[93] Wichtmann T, Triantafyllidis T. Monotonic and cyclic tests on kaolin: a database for the development, calibration and verification of constitutive models for cohesive soils with focus to cyclic loading. Acta Geotech 2018;13:1103–28. https://doi.org/10.1007/s11440-017-0588-3.

[94] Cavounidis S. On the ratio of factors of safety in slope stability analyses. Géotechnique 1987;37:207–10. https://doi.org/10.1680/geot.1987.37.2.207.

[95] Gao Y, Zhang F, Lei GH, Li D, Wu Y, Zhang N. Stability Charts for 3D Failures of Homogeneous Slopes. J Geotech Geoenvironmental Eng 2013;139:1528–38. https://doi.org/10.1061/(ASCE)GT.1943-5606.0000866.

[96] Griffiths DV, Fenton GA. Probabilistic Slope Stability Analysis by Finite Elements. J Geotech Geoenvironmental Eng 2004;130:507–18. https://doi.org/10.1061/(ASCE)1090-0241(2004)130:5(507).

[97] Hicks MA, Samy K. Influence of heterogeneity on undrained clay slope stability. Q J Eng Geol Hydrogeol 2002;35:41–9. https://doi.org/10.1144/qjegh.35.1.41.

[98] Phoon K-K, Kulhawy FH. Characterization of geotechnical variability. Can Geotech J 1999;36:612–24. https://doi.org/10.1139/t99-038.

[99] Xiong M, Huang Y. A review of time-dependent reliability analyses of slopes: Research progress, influencing factors, and future research directions. Transp Geotech 2022;37:100867. https://doi.org/10.1016/j.trgeo.2022.100867.

[100] Smethurst JA, Briggs KM, Powrie W, Ridley A, Butcher DJE. Mechanical and hydrological impacts of tree removal on a clay fill railway embankment. Géotechnique 2015;65:869–82. https://doi.org/10.1680/jgeot.14.P.010.

[101] Alexander LV, Jones PD. Updated precipitation series for the U.K. and discussion of recent extremes. Atmospheric Sci Lett 2000;1:142–50. https://doi.org/10.1006/asle.2000.0016.

[102] Murphy JM, Harris GR, Sexton DMH, Kendon EJ, Bett PE, Clark RT, et al. UKCP18 Land Projections: Science Report. Exeter: Met Office Hadley Centre; 2018.

[103] Alonso EE, Gens A, Delahaye CH. Influence of rainfall on the deformation and stability of a slope in overconsolidated clays: a case study. Hydrogeol J 2003;11:174–92. https://doi.org/10.1007/s10040-002-0245-1.

[104] Oh S, Lu N. Slope stability analysis under unsaturated conditions: Case studies of rainfall-induced failure of cut slopes. Eng Geol 2015;184:96–103. https://doi.org/10.1016/j.enggeo.2014.11.007.